



Transcriptome-scale spatial gene expression in the human dorsolateral prefrontal cortex

Kristen R. Maynard^{1,2,10}, Leonardo Collado-Torres^{1,3,10}, Lukas M. Weber⁴, Cedric Uytingco⁵, Brianna K. Barry^{1,6}, Stephen R. Williams⁵, Joseph L. Catallini II⁴, Matthew N. Tran^{1,7}, Zachary Besich^{1,7}, Madhavi Tippani¹, Jennifer Chew⁵, Yifeng Yin⁵, Joel E. Kleinman^{1,2}, Thomas M. Hyde^{1,2,8}, Nikhil Rao⁵, Stephanie C. Hicks^{1,4}, Keri Martinowich^{1,2,6}✉ and Andrew E. Jaffe^{1,2,3,4,6,7,9}✉

We used the 10x Genomics Visium platform to define the spatial topography of gene expression in the six-layered human dorsolateral prefrontal cortex. We identified extensive layer-enriched expression signatures and refined associations to previous laminar markers. We overlaid our laminar expression signatures on large-scale single nucleus RNA-sequencing data, enhancing spatial annotation of expression-driven clusters. By integrating neuropsychiatric disorder gene sets, we showed differential layer-enriched expression of genes associated with schizophrenia and autism spectrum disorder, highlighting the clinical relevance of spatially defined expression. We then developed a data-driven framework to define unsupervised clusters in spatial transcriptomics data, which can be applied to other tissues or brain regions in which morphological architecture is not as well defined as cortical laminae. Last, we created a web application for the scientific community to explore these raw and summarized data to augment ongoing neuroscience and spatial transcriptomics research (<http://research.libd.org/spatialLIBD>).

The spatial organization of the brain is fundamentally related to its function. This structure–function relationship is especially apparent in the context of the laminar organization of the human cerebral cortex, in which cells residing within different cortical layers show distinct gene expression patterns and exhibit differing patterns of morphology, physiology and connectivity^{1–4}. To the extent that structure entrains function, understanding normal brain development as well as disorders of the central nervous system will require identification of the cell types that make up the brain, and ultimately link functional correlates of individual cell classes with structural architecture.

Major advances in single-cell RNA-sequencing (scRNA-seq) and single-nucleus (sn)RNA-seq technologies have dramatically increased identification of molecularly defined cell types in the human brain and implicated unique cell classes at risk for specific brain disorders^{5–11}. Although scRNA-seq approaches are common in rodent brain tissue, the relatively large size and fragility of human neurons, coupled with the fact that most available postmortem human brain tissue is frozen, have resulted in nearly all available data in the human brain being generated on isolated nuclei with snRNA-seq approaches¹². Although nuclear profiles are generally representative of whole-cell profiles¹³, isolated nuclei lack the cytoplasmic compartment as well as axons and proximal dendrites, which limits our understanding of gene expression in the cytosol and neuropil¹². This is problematic for studies of brain disorders because converging evidence suggests that impairments in the for-

mation or maintenance of synapses in critical cortical microcircuits are involved in many neuropsychiatric and neurodevelopmental disorders, including schizophrenia disorder (SCZD) and autism spectrum disorder (ASD)^{6,14,15}. Indeed, studies in the postmortem brains of individuals with these disorders have not only implicated specific cell types^{6,12,16}, but also revealed differences in neuronal and synaptic structure that are spatially localized to specific cortical layers^{6,14}. Furthermore, genes associated with increased risk for SCZD that were identified by genome-wide association studies (GWASs) are preferentially enriched for synaptic neuropil transcripts¹², suggesting that the extranuclear information missed by snRNA-seq approaches may be especially relevant for understanding genetic risk for brain disorders. Although molecular profiles derived from sc/snRNA-seq data can be used to predict anatomical location based on canonical marker genes described in the literature or from curated datasets, the precise assignment of gene expression to the spatial coordinates of individual cell populations within intact brain cytoarchitecture of postmortem human brain tissue would substantially advance our understanding of studies of human brain development and disease.

As it is considered a gold standard for quantifying gene expression with high spatial resolution, we recently established and optimized methods for using multiplex single-molecule fluorescent *in situ* hybridization (smFISH) in postmortem human brain tissue¹⁷. However, multiplexing with these technologies is limited and, even for methodologies that can accommodate hundreds

¹Lieber Institute for Brain Development, Johns Hopkins Medical Campus, Baltimore, MD, USA. ²Department of Psychiatry and Behavioral Sciences, Johns Hopkins School of Medicine, Baltimore, MD, USA. ³Center for Computational Biology, Johns Hopkins University, Baltimore, MD, USA. ⁴Department of Biostatistics, Johns Hopkins Bloomberg School of Public Health, Baltimore, MD, USA. ⁵10x Genomics, Pleasanton, CA, USA. ⁶Department of Neuroscience, Johns Hopkins School of Medicine, Baltimore, MD, USA. ⁷Department of Genetic Medicine, McKusick-Nathans Institute of Genetic Medicine, Johns Hopkins University School of Medicine, Baltimore, MD, USA. ⁸Department of Neurology, Johns Hopkins School of Medicine, Baltimore, MD, USA. ⁹Department of Mental Health, Johns Hopkins Bloomberg School of Public Health, Baltimore, MD, USA. ¹⁰These authors contributed equally: Kristen R. Maynard, Leonardo Collado-Torres. ✉e-mail: keri.martinowich@libd.org; andrew.jaffe@libd.org

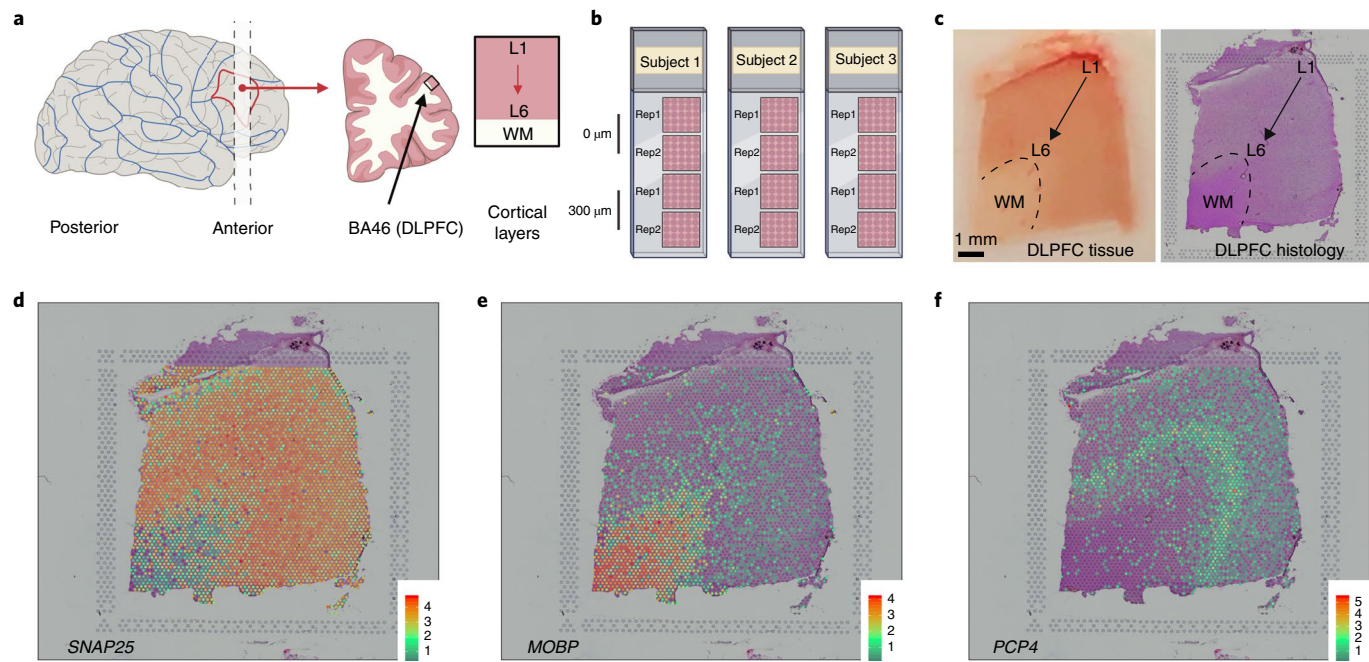


Fig. 1 | Spatial transcriptomics in DLPFC using Visium. **a**, Tissue blocks of DLPFC were acquired in the anatomical plane perpendicular to the pial surface and extended to the gray–white matter junction. Each block spanned the six cortical layers and WM. **b**, Schematic of experimental design including two pairs of spatial replicates from three independent neurotypical adult donors. Each pair consisted of two directly adjacent, 10- μ m serial tissue sections, with the second pair located 300 μ m posterior to the first, resulting in a total of 12 samples run on the Visium platform. **c**, DLPFC tissue block and corresponding histology from sample 151673. **d–f**, Spotplots depicting log(transformed normalized expression) (log(counts)) for sample 151673 for genes SNAP25 (**d**), MOBP (**e**) and PCP4 (**f**). Expression of these genes confirmed the spatial orientation of each sample by delineating the border between gray matter/neurons (SNAP25) and WM/oligodendrocytes (MOBP) and defining L5 (PCP4). Spotplots of SNAP25, MOBP and PCP4 for all 12 samples can be found in Supplementary Figs. 2 and 3 and Extended Data 1. See also Supplementary Table 1.

to thousands of transcripts simultaneously, molecular crowding within cells leads to fluorescence overlap, which introduces notable microscopy-related issues and computational challenges^{18,19}. The relatively large size of the human brain and lipofuscin-derived auto-fluorescence pose additional challenges for microscopy-based spatial transcriptomic methods in postmortem human tissue. Although methods such as laser capture microdissection sequencing do allow for transcriptome-wide profiling from cytosol in a spatially defined area^{20–22}, the tissue is removed from the surrounding spatial context and processed separately, hindering the ability to analyze gradients of gene expression and examine spatial relationships within intact sections.

Emerging technologies for genome-wide spatial transcriptomics offer great potential for providing detailed molecular maps that overcome limitations associated with sn/scRNA-seq and microscopy-based spatial transcriptomics methods. Importantly, these technologies use an on-slide complementary DNA synthesis approach that captures gene expression in the architecture of intact tissue, meaning that information from cytosol and neuronal processes is retained^{23,24}. To further our understanding of gene expression within the context of the spatial organization of the human cortex, we used the recently released 10x Genomics Visium platform, a new barcoding-based, transcriptome-wide, spatial transcriptomics technology, to generate spatial maps of gene expression in the six-layered dorsolateral prefrontal cortex (DLPFC) of the adult human brain. The Visium platform expands the spatial resolution fivefold beyond the first-generation spatial transcriptomics approach²³ on which it is based. Although the original approach was successfully used to generate gene expression atlases and identify perturbations in transcriptional pathways for several normal and pathological human tissues, including the developing heart²⁵, invasive ductal cancer²³, pancreatic ductal adenocarcinoma²⁶, prostate

cancer²⁷, postmortem spinal cord²⁸ and cerebellum²⁹ of patients with amyotrophic lateral sclerosis, it lacked the necessary spatial resolution to resolve both individual cells and laminar structures in the human cortex.

As some differences in pathology and gene expression associated with neuropsychiatric disorders are localized to specific cortical layers^{6,14}, the ability to localize spatial gene expression in the human brain at cellular resolution will be critical to gain further insight into disease mechanisms. Toward this end, we sought to define the laminar topography of gene expression in the human DLPFC, a brain area that has been implicated in a number of neuropsychiatric disorders. We overlaid data from recent large-scale snRNA-seq studies in the human brain with our spatial data to first confirm our layer-enriched expression signatures, and then increase precision in manual annotation of gene expression-driven clusters to cortical laminae. To exemplify the potential of this type of data for clinical translation, we integrated our dataset with various neuropsychiatric disorder gene sets to demonstrate preferential layer-enriched expression of ASD risk genes and layer-enriched association of risk for several neuropsychiatric disorders. Finally, we compared the manually annotated laminar clusters to entirely data-driven spatial clusters in the same human cortical tissue, using an approach that can also be applied to other human tissues and brain regions that do not have as clear a morphological patterning as the cerebral cortex. We provide these data and analysis tools as a scientific resource for the neuroscience community to augment current molecular profiling and spatial transcriptomics efforts in the human brain.

Results

We profiled spatial gene expression in human postmortem DLPFC tissue sections from two pairs of ‘spatial replicates’ from three independent neurotypical adult donors. Each pair consisted of two

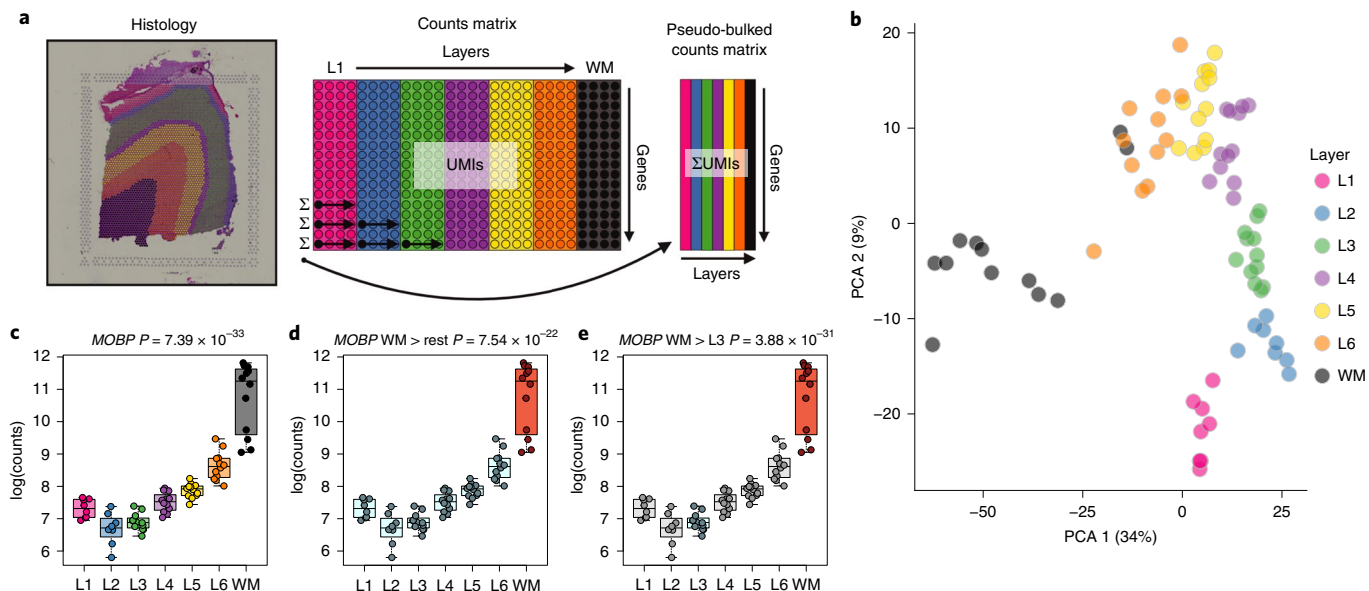


Fig. 2 | Layer-enriched gene expression in the DLPFC. **a**, Visual description of the pseudo-bulking statistical procedure, which collapses the spatial transcriptomics data from spot-level (~4,000 spots) to layer-level (six layers + WM) data within each tissue section. **b**, PCA of layer-level (pseudo-bulked) expression profiles across all sections and subjects. The first PC separates the WM and gray matter, and the second PC associates with laminae. **c–e**, Visual depictions of the three statistical models employed to assess laminar enrichment, using *MOBP* as an example, including the ANOVA model (**c**), which tests whether the means of the seven layers are different, the enrichment model (**d**), which tests whether each layer differs from all other layers (shown is WM (orange) versus other six layers (light blue)), and the pairwise model (**e**), which tests each layer versus each other layer (shown in WM (orange) versus L3 (light blue), with other layers in gray). The 76 pseudo-bulked layers were used for computing the statistics in **c–e**. See also Supplementary Fig. 5, Extended Data Figs. 2 and 4 and Supplementary Table 4.

directly adjacent, 10-μm serial tissue sections with the second pair located 300 μm posterior to the first, resulting in a total of 12 samples run on the Visium platform (Fig. 1a,b, Supplementary Table 1 and Supplementary Fig. 1). We sequenced each sample to a median depth of 291.1×10^6 reads (interquartile range (IQR) 269.3×10^6 – 327.7×10^6), which corresponded to a mean of 3,462 unique molecular identifiers (UMIs) and a mean of 1,734 genes per spot. We note that these rates are analogous to snRNA-seq and scRNA-seq data using the 10x Genomics Chromium platform, where a ‘cell’ barcode on the Chromium platform corresponds to a ‘spatial’ barcode on the Visium platform. However, unlike snRNA-seq data from postmortem human brain, which contains high numbers of intronic reads that map to immature transcripts, we found strong enrichment of mature messenger RNAs with high mean rates of exonic alignments (mean: 83.3%; IQR: 82.5–84.3%). Independent processing and cell segmentation of high-resolution histology images acquired before on-slide cDNA synthesis indicated an average of 3.3 cells per spot (IQR: 1–4), with a mean 15.0% (IQR: 12.8–17.9%) spots per sample containing a single cell body and 9.7% (IQR: 5.4–12.3%) neuropil spots that lacked any cell bodies. Tissue sections were acquired in the plane perpendicular to the pial surface that extended to the gray–white matter junction (Fig. 1c). The orientation of each sample was confirmed by delineating the border between layer 6 (L6) and the adjacent white matter (WM) and identifying layer L5, using marker genes for gray matter/neurons (*SNAP25*), WM/oligodendrocytes (*MOBP*) and L5 (*PCP4*) in each tissue section (Fig. 1d–f, Supplementary Figs. 2 and 3, and Extended Data Fig. 1). A summary of the data generated and analyses performed is located in Supplementary Fig. 4.

Gene expression in the DLPFC across cortical laminae. We first generated aggregated layer-enriched expression profiles for each spatial replicate using a ‘supervised’ approach to assign

individual spots to each of the six neocortical layers or the WM (Supplementary Fig. 5). Then, we performed ‘pseudo-bulking’ by summing the UMI counts for each gene within each layer across each spatial replicate to generate layer-enriched expression profiles (Fig. 2a). The pseudo-bulking approach, summarizing 47,681 spots to 76 layer-aggregated profiles across the 12 samples, removed sparsity and greatly increased UMI coverage of genes (Fig. 2a). Unsupervised clustering of these layer-enriched expression profiles revealed the top component of variation in the data related to laminar differences, particularly between the WM and gray matter (Fig. 2b), with high concordance between the pairs of spatial replicates (Extended Data 2). Segmentation of histological images confirmed sparser cell densities in layer 1 (L1), a molecular layer enriched in synaptic processes, with 33.4% and 21.7% of spots containing 0 and 1 cell body, respectively. We observed increased cell densities in the oligodendrocyte-enriched WM, with 3.9% and 5.9% of spots containing 0 and 1 cell body, respectively (Supplementary Table 2). We hypothesized that these ‘neuropil spots’ with 0 cell bodies may be enriched with neuronal processes (that is, axons and dendrites; Supplementary Table 3), and as predicted we identified significant enrichment of genes that are preferentially expressed in the transcriptome of synaptic terminals³⁰ (Spearman’s $\rho=0.38$, $P=1.9 \times 10^{-30}$; Extended Data Fig. 3). Together, these analyses demonstrate the power of concurrently acquiring histology and gene expression data, and highlight the ability of the Visium platform to achieve high-resolution spatial expression profiling within the human DLPFC.

We used three strategies to perform differential expression (DE) analyses using the layer-enriched expression profiles generated above with linear mixed-effects modeling (Extended Data 4). The first strategy involved testing for differences in mean expression across the six layers plus WM (we also tested for differences in mean expression with only six layers, excluding WM), termed the

'ANOVA (analysis of variance) model' (Fig. 2c), which estimates an *F* statistic for each gene. This strategy revealed extensive DE across the laminar organization of the DLPFC, with 10,633 (47.6%) DE genes (DEGs) across the six gray matter layers plus WM (at a false discovery rate (FDR) < 0.05) and 8,581 (38.4%) DEGs across the six gray matter layers excluding WM (FDR < 0.05). As expected, these results suggested extensive differences in gene expression between the layers of the DLPFC beyond broad WM versus gray matter comparisons. The second strategy identified layer-enriched genes by testing for differences in expression between one layer versus all other layers, termed the 'enrichment' model (Fig. 2d), which resulted in a Student's *t*-test statistic (termed 'layer-enriched statistics' hereafter) and *P* value (and corresponding FDR-adjusted *q* value) for each expressed gene and layer. The largest expression differences were between WM and the neocortical layers, with 9,124 DEGs (FDR < 0.05), and the smallest differences were between L3 and all other layers with 183 DEGs (Supplementary Table 4). In the third strategy, we tested for genes differentially expressed between each pair of layers (21 pairs), termed the 'pairwise' model (Fig. 2e), which produced significant DEGs ranging from 8,500 for WM versus L3 to 292 for L4 versus L5 (Supplementary Table 4). Together, these analyses highlight the extensive gene expression differences between the different layers of the human adult DLPFC.

Identifying new layer-enriched genes in human cortex. Several resources have compiled genes that exhibit laminar-specific expression across both rodent³¹ and human cortices³². Although both overlapping and unique marker genes have been identified, these studies used different technologies, examined different developmental stages and queried different regions of the cortex. Therefore, we systematically assessed the robustness of these previously identified marker genes in our human adult DLPFC-layer-enriched gene expression dataset. First, we tested for enrichment of previously published layer-enriched genes, as a set, among our layer-enriched DEGs, and found strong enrichment ($P=1.22 \times 10^{-41}$). As many of these marker genes were previously annotated to multiple layers (that is, *CCK* and *ENCL*; Fig. 3), rather than a single layer as queried in our DE analyses, we fit the optimal statistical model for each gene using our layer-enriched expression profiles (Supplementary Table 5). For example, *CCK* was annotated to L2, L3 and L6, which were together tested against combining L1, L3, L4 and WM in this optimal model. Only a subset of previously associated layer-enriched genes showed high ranks and significant DE in our human DLPFC data (Extended Data 5), which were largely driven by markers identified by Zeng et al.³².

We further confirmed laminar enrichment of a number of canonical marker genes, including *CCK*, *ENCL*, *CUX2*, *RORB* and *NTNG2*, and validated these findings against publicly available singleplex *in situ* hybridization (ISH) data from the Allen Brain Institute's Human Brain Atlas³³ (Fig. 3 and Extended Data Fig. 6). It is interesting that, although many of these genes (*FABP7*, *ADCYAP1* and *PVALB*) showed layer-enriched expression in our data, they were not classified by the Allen Brain Institute's resources as being layer markers, demonstrating the utility of quantitative transcriptome-scale spatial approaches. Although we confirmed several canonical layer-enriched/specific genes, we found that

only 59.5% of previously identified marker genes were significant DEGs (FDR < 0.05) in human DLPFC (Supplementary Table 5). Indeed, we identified several genes previously underappreciated as laminar markers in human DLPFC, including *AQP4* (L1), *HPCAL1* (L2), *FREM3* (L3), *TRABD2A* (L5) and *KRT17* (L6) (Fig. 4 and Extended Data Fig. 7). We validated these new layer-enriched DEGs using multiplex smFISH (Fig. 4 and Supplementary Fig. 6). New layer-enriched DEGs were also validated by multiplexing with previously identified layer markers in the literature, many of which were also replicated in our Visium data (Supplementary Fig. 7).

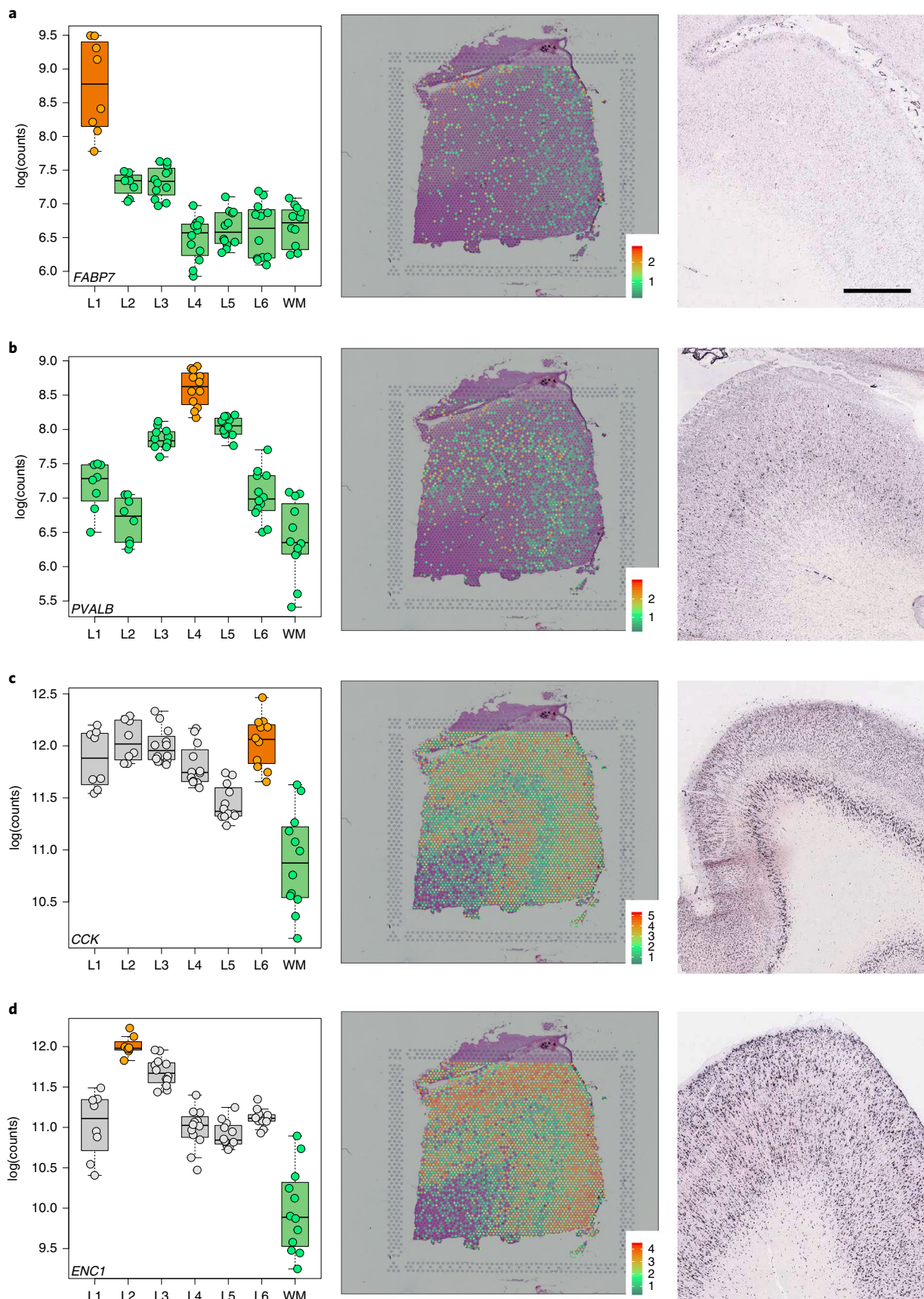
Spatial registration of snRNA-seq. Adding spatial resolution to snRNA-seq datasets generated from human brain tissue has the potential to provide further insights about the function of molecularly defined cell types. Specifically, layer-enriched expression profiles and DE statistics derived from the 'enrichment model' in our Visium data can be used to spatially 'register' snRNA-seq datasets and add layer-enriched information to data-driven expression clusters that do not contain inherent anatomical information (Fig. 5a). We first used snRNA-seq data from Hodge et al.⁵ to confirm our layer-enriched expression profiles and validate this spatial registration strategy. Although the snRNA-seq data in that study were obtained predominantly from NeuN⁺-sorted neuronal nuclei that were isolated from manually dissected layers of the human, postmortem, middle temporal gyrus cortex, our layer-enriched DEGs from spatially barcoded bulk tissue sections were in agreement with the laminar assignments from which these nuclei were derived (Fig. 5b). We further validated this strategy on bulk RNA-seq data that were generated from manually dissected laminar serial sections of the human PFC from four donors²². These data, however, lacked corresponding histology data to definitively annotate specific cortical layers, and assignment of sections to layers probably underestimated the amount of WM present (approximately five sections per sample instead of just one predicted section) and missed L1 in one of their four subjects (H1) (Supplementary Fig. 8).

We then used our layer-enriched statistics to perform spatial registration across three independent snRNA-seq datasets from human cortex. First, we generated our own snRNA-seq data from DLPFC using 5,231 nuclei from two donors, and performed data-driven clustering to generate 30 preliminary cell clusters across 7 broad cell types (Supplementary Fig. 9). Integration of our layer-enriched statistics refined excitatory and inhibitory neuronal subclasses into upper and deep layer subgroups beyond expected enrichments of glial cells in the WM (Extended Data Fig. 8a). We further assessed the robustness of this approach by reanalyzing processed snRNA-seq from 48 donors across 70,634 nuclei obtained from the human PFC (BA10) across 44 broad clusters in a study of Alzheimer's disease¹⁰. Glial cell subpopulations showed expected enrichments, with preferential expression of oligodendrocyte subtypes in the WM, astrocyte subtypes in L1, and microglia, oligodendrocyte precursor, pericytes and endothelial subtypes in both L1 and WM (Fig. 5c). Neuronal cell subtypes showed greater laminar diversity, with multiple excitatory and inhibitory neuronal cell types associating with L2/L3, L4, L5 and L6 preferential expression, with generally more layer-enriched expression within excitatory cells (Fig. 5c). It is interesting that our analysis showed that the excitatory

Fig. 3 | Visium replicates layer enrichment of previously identified layer-marker genes. **a–d**, Left: boxplots of log(transformed normalized expression) (log(counts)) for genes *FABP7* (a, L1 > rest, $P=5.01 \times 10^{-19}$), *PVALB* (b, L4 > rest, $P=1.74 \times 10^{-9}$), *CCK* (c, L6 > WM, $P=4.48 \times 10^{-19}$) and *ENCL* (d, L2 > WM, $P=4.61 \times 10^{-25}$). Middle: spotplots of log(transformed normalized expression) (log(counts)) for sample 151673 for genes *FABP7* (a), *PVALB* (b), *CCK* (c) and *ENCL* (d). Right: ISH images from temporal cortex (a and d), DLPFC (b) or visual cortex (c) of adult human brain from the Allen Human Brain Atlas³³ (<http://human.brain-map.org>). Boxplots and spotplots can be reproduced using our web application at <http://spatial.libd.org/spatialLIBD>. Scale bar (for Allen Brain Atlas ISH images), 1.6 mm. The 76 pseudo-bulked layers were used for computing the statistics in a–d. See also Extended Data Fig. 6 and Supplementary Table 5.

neuronal subclasses (Ex2, Ex4, Ex6) identified by Mathys et al.¹⁰ that were most associated with clinical traits of Alzheimer's disease were preferentially localized to the upper layers (L2/L3) of DLPFC

in our data. This finding contrasts with the inferences that were drawn by Mathys et al.¹⁰, which made layer assignments based on data obtained from the serial sections in He et al.²² described above.



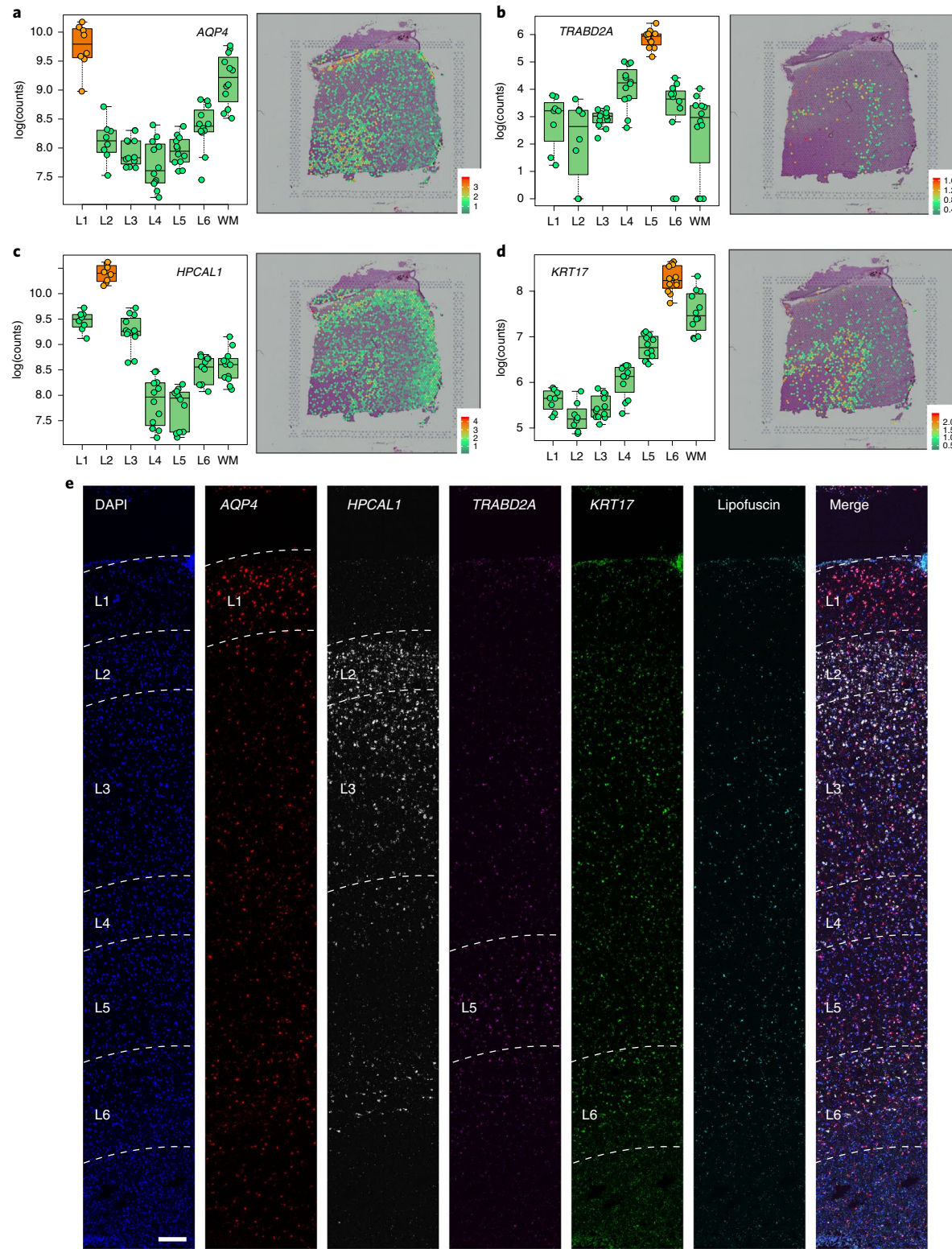


Fig. 4 | Discovery and smFISH validation of new layer-enriched genes. **a-d**, Left: boxplots of log(transformed normalized expression) (log(counts)) for genes *AQP4* (**a**, L1 > rest, $P = 1.47 \times 10^{-10}$), *TRABD2A* (**b**, L5 > rest, $P = 4.33 \times 10^{-12}$), *HPCAL1* (**c**, L2 > rest, $P = 9.73 \times 10^{-11}$) and *KRT17* (**d**, L6 > rest, $P = 5.05 \times 10^{-12}$). Middle: spotplots of log(transformed normalized expression) (log(counts)) for sample 151673 for genes *AQP4* (**a**), *TRABD2A* (**b**), *HPCAL1* (**c**) and *KRT17* (**d**). **e**, Multiplex smFISH in a cortical strip of DLPFC. Maximum intensity confocal projections depict expression of DAPI (nuclei), *AQP4*, *HPCAL1*, *TRABD2A*, *KRT17* and lipofuscin autofluorescence. The merged image is without lipofuscin autofluorescence. Scale bar, 200 μ m. The 76 pseudo-bulked layers were used for computing the statistics in **a-d**. See also Extended Data Fig. 7 and Supplementary Figs. 6 and 7.

Specifically, they concluded that excitatory neuronal subclasses Ex4 and Ex6 were preferentially expressed in the deeper layers, whereas excitatory neuronal subclass Ex2 showed no laminar enrichment.

Last we applied our spatial registration analysis to a study of ASD⁶ including snRNA-seq data from 104,559 nuclei isolated from the human PFC and anterior cingulate cortex that were obtained

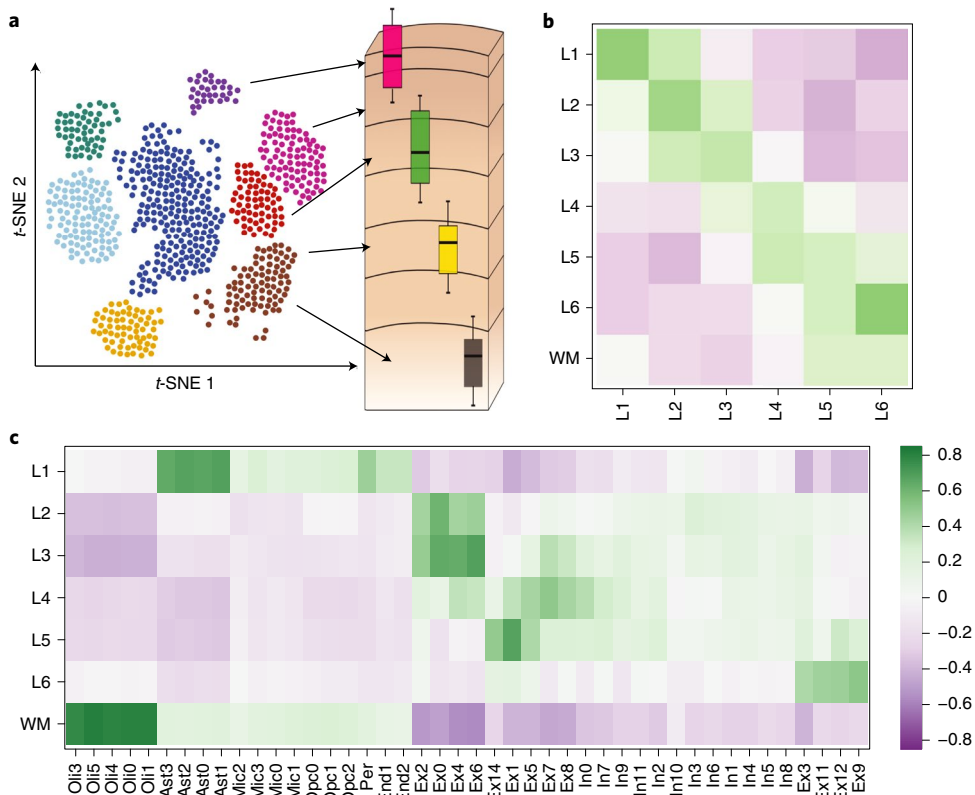


Fig. 5 | Spatial registration of snRNA-seq data. **a–c**, Overview of the spatial registration approach. Heatmap of Pearson’s correlation values evaluates the relationship between our derived layer-enriched statistics (y axis) for 700 genes (**a**), layer-enriched statistics from snRNA-seq data in human medial temporal cortex produced by Hodge et al.⁵ (**b**; these data only profiled layers 1–6 in the gray matter, x axis) and cell-type-specific statistics for cellular subtypes that were annotated by Mathys et al. from snRNA-seq data in the human PFC¹⁰ (**c**; x axis). Ast, astrocyte; End, endothelial; Ex, excitatory neurons; In, inhibitory neurons; Mic, microglia; Oli, oligodendrocyte; Opc, oligodendrocyte precursor cell; Per, pericyte. See also Supplementary Figs. 8 and 9 and Extended Data Fig. 8.

from 41 samples across 31 donors, which were annotated to 17 clusters in a study of ASD⁶ (Extended Data Fig. 8b). As expected, we confirmed expected spatial contexts; for example, the highest enrichment of oligodendrocytes was again found in our histologically defined WM. Our spatial registration framework was also able to refine the laminar predictions of cell types in these previous studies. For example, integration of layer-enriched genes defined by Visium with snRNA-seq data from Velmeshev et al.⁶ indicated that astrocyte populations were most enriched in L1, whereas excitatory neurons annotated to L4 were more likely to be found in L5. These analyses demonstrate how this spatial registration framework can be readily applied to any existing snRNA-seq or scRNA-seq datasets from dissociated cells to add back anatomical information.

Clinical relevance of layer-enriched gene expression profiling. Given that several studies have identified associations between different brain disorders and molecularly defined cell types, we assessed the clinical relevance of spatial gene expression using several different brain disorder-associated gene sets. We assessed the laminar enrichment of: (1) gene sets derived from genes linked to different disorders via DNA profiling; (2) genes differentially expressed in postmortem brains of patients with a variety of brain disorders and neurotypical controls; and (3) genes associated with genetic risk via transcriptome-wide association studies (TWASs). We first used broad gene sets for different brain disorders compiled by Birnbaum et al.³⁴, which showed laminar enrichments specifically for ASD (Supplementary Fig. 10 and Supplementary Table 6). We used the latest SFARI Gene database³⁵ to refine these associations, and demon-

strate enrichments of L2 (odds ratio (OR)=2.74, $P=6.0\times 10^{-21}$), L5 (OR=2.1, $P=8.7\times 10^{-7}$) and L6 (OR=2.7, $P=1.8\times 10^{-7}$) with ASD risk genes (Fig. 6a). We confirmed the L2 (OR=3.6, $P=3.9\times 10^{-6}$) and L5 (OR=4.0, $P=6.7\times 10^{-5}$) associations in a recent exome sequencing study by Satterstrom et al.³⁶, which identified 102 genes with ASD-associated variants. It is interesting that stratifying these genes by their clinical symptoms refined the laminar enrichments, because the 53 genes associated with ASD-dominant traits were more enriched for L5 (OR=4.9, $P=5.3\times 10^{-4}$, 8 genes: *TBR1*, *SATB1*, *ANK2*, *RORB*, *MKX*, *CELF4*, *PPP5C* and *AP2S1*), whereas the 49 genes associated with neurodevelopmental delay were more enriched for L2 (OR=4.5, $P=7.8\times 10^{-5}$, 12 genes: *CACNA1E*, *MYT1L*, *SCN2A*, *TBL1XR1*, *NR3C2*, *SYNGAP1*, *GRIN2B*, *IRF2BPL*, *GABRB3*, *RAII*, *TCF4* and *ADNP*), suggesting that different functional subclasses of neurons might be contributing to each clinical subgroup. These layer-enriched expression associations for risk genes were largely independent of the enrichments seen comparing genes more highly expressed (WM, $P=1.9\times 10^{-29}$ and L1, $P=4.5\times 10^{-61}$) or more lowly expressed (L3, $P=2.9\times 10^{-5}$; L4, $P=1.7\times 10^{-42}$; L5, $P=3.2\times 10^{-36}$; and L6, $P=1.9\times 10^{-7}$) in brains of ASD patients compared with neurotypical controls (Supplementary Table 6).

We further assessed laminar enrichment of genes proximal to common genetic variation associated with SCZD, ASD, bipolar disorder (BPD) and major depressive disorder³⁷. These analyses identified significant overlap between L2-enriched and L5-enriched genes and risk for SCZD (at Bonferroni’s <0.05), with additional overlap between L2-enriched genes and risk for BPD (at FDR <0.05 ;

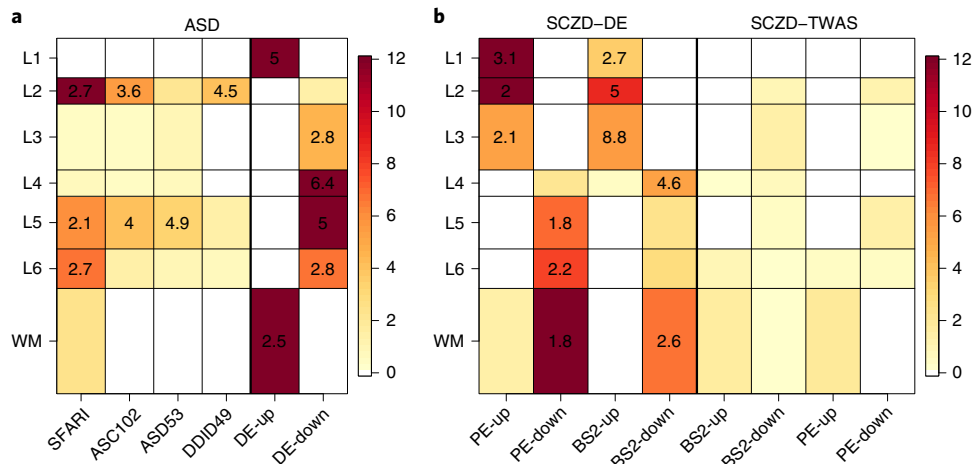


Fig. 6 | Layer enrichment of neurodevelopmental and neuropsychiatric gene sets. We performed enrichment analyses using Fisher's exact tests for our layer-enriched statistics versus a series of predefined related gene sets. **a**, ASD laminar enrichments for SFARI³⁵ and Satterstrom et al.³⁶ for 102 overall ASD genes (ASC102), which were further stratified into 53 predominantly ASD (ASD53) and 49 predominantly developmental delay (DDID49) genes, as well as genes differentially expressed in the brains of individuals with ASD versus neurotypical controls, as reported in the Gandal et al. psychENCODE (PE) study¹⁶. **b**, SCZD genes, including those from DE and TWAS analyses of RNA-seq data from brains of individuals with SCZD compared with neurotypical controls in the BrainSeq (BS)³⁸ and PE¹⁶ studies. The 'up' and 'down' labels indicate whether genes are more highly or lowly expressed, respectively, in individuals with ASD or SCZD compared with neurotypical controls. Color scales indicate $-\log_{10}(P)$, which were thresholded at $P=10^{-12}$, and numbers within significant heatmap cells indicate ORs for the enrichments. See also Supplementary Fig. 10 and Supplementary Tables 6–8.

Supplementary Table 7). As above with ASD, there were markedly different laminar enrichments for genes associated with the SCZD illness state. Enrichment analyses of DEGs identified in two large SCZD postmortem brain datasets^{16,38}, although highly convergent across studies, showed extensive enrichment across all layers, with increased expression of L1, L2 and L3 genes and decreased expression of WM, L4, L5 and L6 genes in patients compared with controls (Fig. 6b). As secondary analyses, we performed heritability partitioning analysis³⁹ for layer-enriched gene sets, which again identified significant heritability enrichment exclusively for L2-enriched genes, specifically for SCZD, BPD and educational attainment (Supplementary Table 8). We also assessed TWAS statistics constructed for SCZD and BPD from SNP weights computed from DLPFC^{16,20}. Although we did not observe strong enrichments of the TWAS signal for any layer-enriched gene expression, SCZD risk genes in L2 and L5 suggested decreased expression in illness (Fig. 6b and Supplementary Table 6). Together, these analyses highlight the potential utility of these data in gleaning clinical insights by incorporating layer-enriched gene expression of the adult DLPFC into the interpretation of risk genes.

Data-driven, layer-enriched clustering in the DLPFC. Last, we explored the use of three alternative data-driven approaches to classify Visium spots into laminar and nonlaminar patterns, in contrast to the supervised approach of identifying layer-enriched DEGs from manual annotation of layers based on cytoarchitecture (Fig. 7a,b and Supplementary Fig. 11), which may not be feasible in other brain regions or human tissues that lack clear or established morphological boundaries. Toward this goal, we explored the use of two gene sets: (1) genes exhibiting spatially variable expression patterns (SVGs) within each of the 12 samples (Supplementary Table 9) and (2) highly variable genes (HVGs). Although no laminar information was used to identify SVGs and HVGs, it is interesting that these gene sets could identify both laminar and nonlaminar spatial patterns (Fig. 7c,d). For example, we identified several SVGs that were nonlaminar, including *HBB*, *IGKC* and *NPY*, which probably relate to blood cells, immune cells and inhibitory interneuron classes (Fig. 7d). In a completely data-driven and unsupervised approach,

we then used several implementations of unsupervised clustering methods with spot-level Visium data using these gene sets, with the possibility of further incorporating spatial coordinates of the spots, because we reasoned that adjacent spots should tend to show expression levels with greater similarity (Fig. 7e, and Extended Data Figs. 9 and 10). We compared these results with a semi-supervised approach (unsupervised clustering guided by the layer-enriched genes identified using the DE enrichment models; Extended Data Fig. 4) and an approach using known rodent and human layer marker genes from Zeng et al.³² (Fig. 7e and Supplementary Table 10).

Using the manually annotated layers as a gold standard (Fig. 7a and Supplementary Fig. 11), we evaluated the performance of the three approaches (unsupervised, semi-supervised and markers) using the adjusted Rand index (ARI) as the performance metric. Specifically, the ARI measures the similarity between the predicted cluster labels from our three approaches and the gold standard cluster labels, with higher values corresponding to better performance (Fig. 7f). First, we found consistent, but moderate, performance improvements by incorporating *x* and *y* spatial coordinates of the spots into the clustering methods across all three approaches (Fig. 7f). Within the unsupervised approach, we found that using the HVGs resulted in the highest ARI, but with the SVGs also comparable in performance (Fig. 7f). However, the semi-supervised approach resulted in the highest ARI out of all three approaches. This probably stems from the circularity of performing data-driven clustering guided by our layer-enriched DEGs on the same data, but this could be powerful in future spatial transcriptomics studies in the human cortex.

Discussion

Based on examination of its histological organization and cytoarchitecture, the neocortex can be divided into six layers, which can be differentiated based on cell-type composition and density, as well as morphology and connectivity of resident cell types^{1–4}. Studies of postmortem brains from individuals with neuropsychiatric disorders have identified disease-associated changes in gene expression and synaptic structure that can be localized to individual layers^{5,14}.

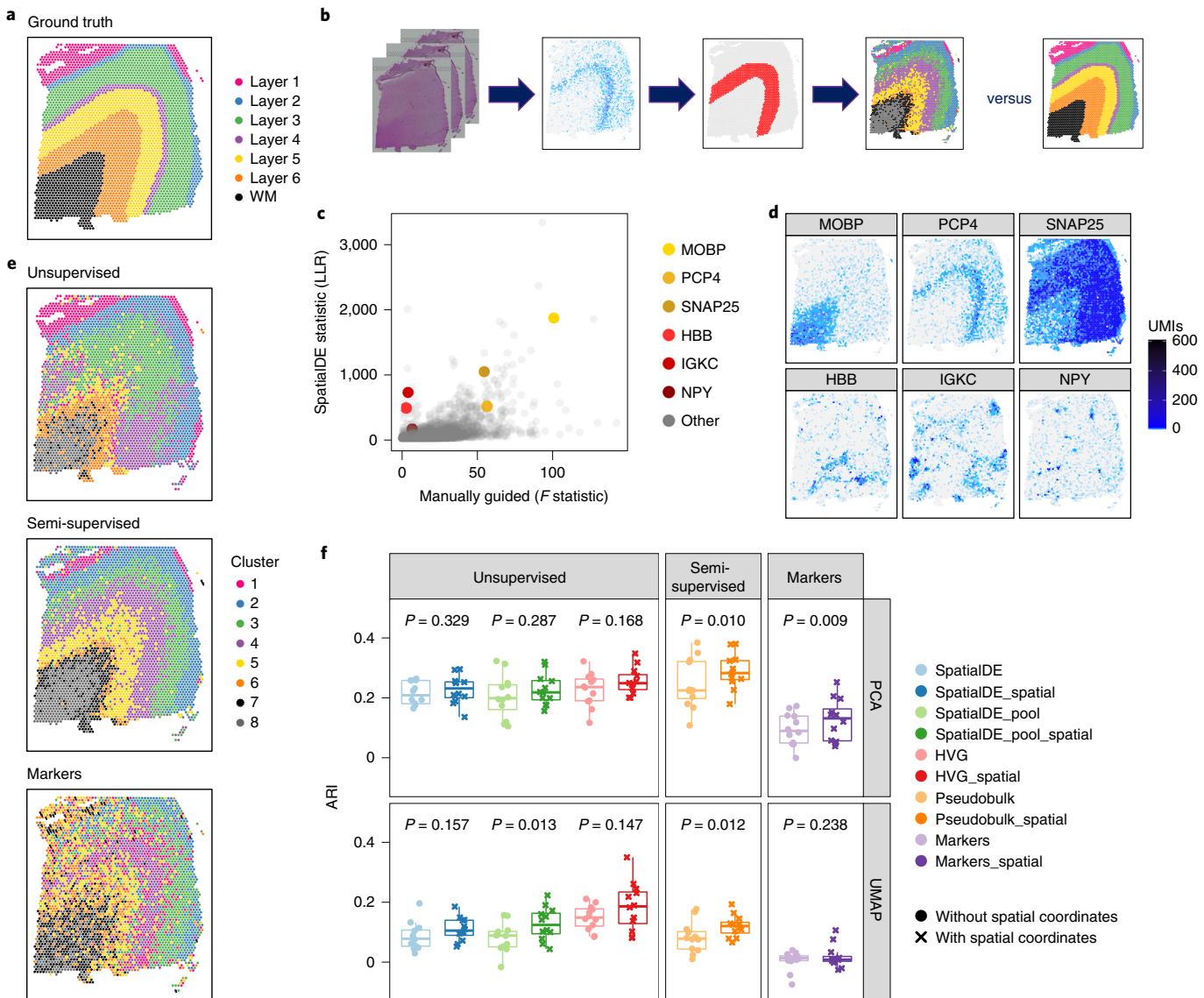


Fig. 7 | Data-driven, layer-enriched clustering in the DLPFC. **a**, Supervised annotation of DLPFC layers based on cytoarchitecture and selected gene markers (as shown in Fig. 2a), used as ‘ground truth’ to evaluate the data-driven clustering results, for sample 151673. **b**, Schematic illustrating the data-driven clustering pipeline, consisting of: (1) identifying genes (HVGs or SVGs) in an unbiased manner, (2) clustering on these genes and (3) evaluation of clustering performance by comparing with ground truth. **c**, Comparison of gene-wise test statistics for SVGs identified using SpatialDE ($\log(\text{likelihood ratio})$) and genes from the DE enrichment models (Extended Data Fig. 4) (F statistics; WM included) for sample 151673. Colors indicate selected genes with laminar (yellow shades) and nonlaminar (red shades) expression patterns. LLR, $\log(\text{likelihood ratio})$. **d**, Expression patterns for selected laminar (top row) and nonlaminar (bottom row) genes identified using SpatialDE (corresponding to highlighted genes in **c**) in sample 151673. **e**, Visualization of clustering results for the best-performing implementations of: (1) unsupervised clustering (method ‘HVG_PCA_{spatial}’, which uses HVGs from scran and 50 PCs for dimension reduction and includes spatial coordinates as features for clustering); (2) semi-supervised clustering guided by layer-enriched genes identified using the DE enrichment models; and (3) clustering guided by known markers from Zeng et al.³² (Supplementary Table 10). **f**, Evaluation of clustering performance for all methods across all 12 samples, using manually annotated ground truth layers (as in **a**) and ARI. Points represent each method and sample, with results stratified by clustering methodology (Supplementary Table 10). P values represent statistical significance of the difference in ARI scores when including the two spatial coordinates as features within the clustering, using a linear model fit for each method (overall model across all methods: $P = 5.8 \times 10^{-6}$). See also Supplementary Fig. 11, Extended Data Figs. 9 and 10, and Supplementary Tables 9 and 10.

Our study, among the first to implement Visium technology in human brain tissue, provides a number of important functional insights about the spatial and molecular definitions of cell populations across cortical laminae by analyzing gene expression within the intact spatial organization of the human DLPFC.

First, we demonstrated the potential clinical translation of quantifying layer-enriched expression profiles in human DLPFCs. By integrating our data with clinical gene sets and DEGs in the brains

of individuals with various neuropsychiatric disorders, we demonstrated preferentially layer-enriched expression of the genes implicated in ASD and SCZD. For example, genes that harbor new mutations associated with ASD³⁶ were preferentially expressed in L2 and L5 subsets of these genes associated with specific clinical characteristics and could be further partitioned into specific laminae. Specifically, genes predominantly associated with neurodevelopmental delay were preferentially expressed in L2 and genes

predominantly associated with ASD were preferentially expressed in L5. These specific laminar associations with penetrant new variants were in contrast to broad laminar enrichments of DEGs in the brains of patients with ASD¹⁶ and lack of laminar enrichment of genes implicated by a common genetic variation⁴⁰. It is interesting that these same two layers, L2 and L5, showed preferential enrichment of genes implicated in common variation for SCZD⁴¹, and to a lesser extent BPD⁴². These results were in contrast with DE analyses from postmortem studies of brain tissue from patients with SCZD compared with neurotypical controls^{16,38}, which showed increased expression of upper-layer genes and decreased expression of deep-layer and WM genes. Furthermore, we show that SCZD heritability is enriched in L2, a finding that implicates intracortical information processing as a potential mechanism for genetic risk.

Second, we overlaid recent, large-scale, snRNA-seq data from several cohorts to both confirm our layer-enriched expression signatures and further annotate gene expression-driven clusters to individual cortical layers. The shift from homogenate sequencing studies of brain tissue^{38,43,44} to large-scale snRNA-seq has already begun, with increasing sample sizes and numbers of nuclei^{6,10}. Our spatial registration strategy, which uses individual gene-level statistics from both layer-specific versus cell-type-specific expression profiles from hundreds or thousands of genes is probably more powerful than table-based enrichment analyses using small subsets of previously defined marker genes. Spatial registration of multiple independent datasets with our Visium data showed that layer-enriched patterns of expression can be extracted from snRNA-seq data, as subtypes of excitatory neuronal cells, and, to a lesser extent, inhibitory neuronal cells could be classified by their preferential laminar enrichment. Although this strategy does not aid in constructing cell clusters in snRNA-seq data, it is a powerful tool to better annotate and interpret data-driven clusters, and add spatial context to cell type-specific gene expression in the brain.

Third, in contrast to manually annotating laminar clusters based on cytoarchitecture, which is very labor intensive, we evaluated the performance of alternative, data-driven approaches to cluster spots based on SVGs. Using these data-driven approaches, we identified variable spatial expression related to relatively rare inhibitory neuron subpopulations, brain vasculature and immune function: (1) *NPY*, which encodes a neuropeptide highly expressed in a subpopulation of inhibitory interneurons; (2) *HBB*, which encodes a sub-unit of hemoglobin found in red blood cells; and (3) *IGKC*, which encodes the constant region of immunoglobulin light chains found in antibodies (Fig. 7d). The layer-enriched genes identified in the present study can be used to aid data-driven clustering in human cortex and, indeed, performed better than previously defined markers (Fig. 7e,f). As these data-driven approaches can identify previously unknown cellular organizations, their application will be critical for analyzing other human tissues and brain structures in which morphological patterning is not as well defined or as well characterized compared with the cerebral cortex.

Although laser capture microdissection and other microdissection techniques have been used to generate laminar-specific gene expression profiles in human cortex^{20–22}, morphological boundaries cannot be definitively defined, which hinders the ability to examine spatial relationships between cell populations or to define gradients of gene expression across structures. For example, several layer-enriched genes identified by Visium show striking gradients of gene expression, such as *HPCAL1* which is highly expressed in L2 but steadily decreases in expression through L4, L5 and L6. Conversely, *KRT17* is enriched in L6 and progressively decreases in expression through L5, L4, L3 and L2. Although the current resolution of a spatially barcoded spot in the Visium platform is 55 μm, we found that 15% of spots contained a single cell body, highlighting an additional available level of interrogation for downstream analysis. Ongoing advances will probably lead to improved spatial resolution, because

customized platforms now reach subcellular resolutions of 10 μm and 2 μm^{24,45}. Although each Visium spot may contain a mixture of cell types, incorporating cell body segmentations from histological data can aid in refining interpretations and identifying spots with cell types of interest. Advances in Visium technology that allow for immunofluorescence protein detection can also be used to integrate morphological features of different cell types with gene expression data. Finally, Visium afforded several experimental advantages compared with fluorescence microscopy-based spatial transcriptomics approaches^{46,47}, including: (1) coverage across a large area of brain tissue; (2) unbiased, transcriptome-wide analysis of gene expression (that is, no requirement to select gene targets of interest); and (3) no confounds from lipofuscin autofluorescence. These advantages provide flexibility to analyze spatial gene expression from numerous angles (that is, supervised clustering, unsupervised clustering, neuropil only) within a single experiment, which would be almost impossible to accomplish with more labor-intensive approaches. However, it should be noted that the substantial gyrations inherent to the human cortex make consistency of dissections across individual donors difficult, which will remain a challenge for larger-scale experiments aiming to generate equivalent clusters across tissue sections or perform clustering in a three-dimensional coordinate system. The generation of additional human brain datasets and more finely annotated human brain atlases that include microcircuitry (that is, cortical layers as opposed to cortical regions) will be critical for developing new methods to register snRNA-seq, spatial transcriptomics and accompanying histological data to a common coordinate framework.

Although the laminar structure of the neocortex is largely preserved across mammalian species, several recent studies have underscored key similarities and differences in laminar gene expression across humans, primates and rodents^{5,22,32}. Given the functional importance associated with laminar origin, recent snRNA-seq studies in postmortem human cortex have attempted to annotate molecularly defined cell-type clusters to the layer from which they originated^{6,10}. However, these laminar annotations are largely derived from curated gene sets that come from rodents and nonhuman primates. Although we validated laminar enrichment of some canonical layer-specific genes that were previously identified in the rodent and human cortex (Fig. 3 and Supplementary Fig. 9), some classic markers, such as *BCL11B* (L5), showed weak laminar patterning in adult DLPFC. Likewise, many genes showed no laminar patterning (Extended Data Fig. 5). These findings may represent true differences among brain regions, species and developmental time points, and reinforce previous studies that urge caution in translating rodent and primate studies of molecularly and spatially defined cell types into the human brain. Indeed, our unbiased genome-wide approach identified a number of previously underappreciated layer-enriched genes in human DLPFC, including *HPCAL1* (L2), *KRT17* (L6) and *TRABD2A* (L5), which may represent markers with higher fidelity for laminar annotation of snRNA-seq clusters in the human brain (Fig. 4). We also confirmed laminar enrichment of several genes identified as cell-type markers in specific cortical layers by Hodge et al. (*LAMP5*, *AQP4* and *FREM3*), suggesting conservation between laminar markers in the middle temporal gyrus and DLPFC⁵.

In contrast to the snRNA-seq approaches that encompass the vast majority of gene expression-profiling studies in frozen postmortem human brain tissue, Visium is not limited to analysis of nuclear information. Indeed, on-slide cDNA synthesis methods capture information from both cytosol and neuronal processes, including dendrites and axons (neuropil). Using cell segmentation of high-resolution histology images acquired before on-slide cDNA synthesis, we determined that each spot contained an average of 3.3 cells with 9.7% of spots containing no cell bodies. Confirming our hypothesis that spots containing no cell bodies would be enriched for

transcripts highly expressed in neuronal processes and synapses, we identified significant enrichment of genes preferentially expressed in synaptic terminals. We further found enriched mitochondrial gene expression in sparser layers such as L1 (Supplementary Fig. 12), which probably relates to our finding that L1 was most enriched for neuropil spots, and a higher energetic supply to axons and dendrites would be expected^{48,49}. Moreover, converging evidence suggests that impairments in the formation or maintenance of synapses in key circuits underlie risk for neuropsychiatric disorders and neurodevelopmental delays, including SCZD and ASD^{6,14,15}. Supporting this notion, genes associated with increased risk for SCZD that were identified by GWAS were found to be preferentially enriched for synaptic neuropil transcripts¹². Better understanding of the regulation of synaptically localized transcripts is important because the synaptic proteins they encode control neuronal homeostasis and drive synaptic plasticity⁵⁰, and directly studying neuropil-enriched transcripts in the human brain may provide new insights about expression of locally translated synaptic genes.

Beyond these specific insights, we created several resources for the broader scientific community to continue to interrogate these large datasets for their own biological questions and to extend current neuroscience and spatial transcriptomics research. All raw and processed data and code presented in the present study are freely available through our web application spatialLIBD (<http://spatial.libd.org/spatialLIBD>). Using this application, researchers can visualize the spot-level Visium data, manually annotate spots to layers, visualize the layer-level results, assess the enrichment of gene sets among layer-enriched genes and perform spatial registration. These, and additional features, are described in detail at <http://research.libd.org/spatialLIBD>.

Online content

Any methods, additional references, Nature Research reporting summaries, extended data, supplementary information, acknowledgements, peer review information; details of author contributions and competing interests; and statements of data and code availability are available at <https://doi.org/10.1038/s41593-020-00787-0>.

Received: 12 June 2020; Accepted: 18 December 2020;

Published online: 8 February 2021

References

- DeFelipe, J. & Fariñas, I. The pyramidal neuron of the cerebral cortex: morphological and chemical characteristics of the synaptic inputs. *Prog. Neurobiol.* **39**, 563–607 (1992).
- Harris, K. D. & Shepherd, G. M. G. The neocortical circuit: themes and variations. *Nat. Neurosci.* **18**, 170–181 (2015).
- Narayanan, R. T., Udvary, D. & Oberlaender, M. Cell type-specific structural organization of the six layers in rat barrel cortex. *Front. Neuroanat.* **11**, 91 (2017).
- Radnikow, G. & Feldmeyer, D. Layer- and cell type-specific modulation of excitatory neuronal activity in the neocortex. *Front. Neuroanat.* **12**, 1 (2018).
- Hodge, R. D. et al. Conserved cell types with divergent features in human versus mouse cortex. *Nature* **573**, 61–68 (2019).
- Velmeshev, D. et al. Single-cell genomics identifies cell type-specific molecular changes in autism. *Science* **364**, 685–689 (2019).
- Darmanis, S. et al. A survey of human brain transcriptome diversity at the single cell level. *Proc. Natl Acad. Sci. USA* **112**, 7285–7290 (2015).
- Lake, B. B. et al. Neuronal subtypes and diversity revealed by single-nucleus RNA sequencing of the human brain. *Science* **352**, 1586–1590 (2016).
- Lake, B. B. et al. Integrative single-cell analysis of transcriptional and epigenetic states in the human adult brain. *Nat. Biotechnol.* **36**, 70–80 (2018).
- Mathys, H. et al. Single-cell transcriptomic analysis of Alzheimer's disease. *Nature* **570**, 332–337 (2019).
- Nowakowski, T. J. et al. Spatiotemporal gene expression trajectories reveal developmental hierarchies of the human cortex. *Science* **358**, 1318–1323 (2017).
- Skene, N. G. et al. Genetic identification of brain cell types underlying schizophrenia. *Nat. Genet.* **50**, 825–833 (2018).
- Bakken, T. E. et al. Single-nucleus and single-cell transcriptomes compared in matched cortical cell types. *PLoS ONE* **13**, e0209648 (2018).
- Sweet, R. A., Fish, K. N. & Lewis, D. A. Mapping synaptic pathology within cerebral cortical circuits in subjects with schizophrenia. *Front. Hum. Neurosci.* **4**, 44 (2010).
- Moyer, C. E., Shelton, M. A. & Sweet, R. A. Dendritic spine alterations in schizophrenia. *Neurosci. Lett.* **601**, 46–53 (2015).
- Gandal, M. J. et al. Transcriptome-wide isoform-level dysregulation in ASD, schizophrenia, and bipolar disorder. *Science* **362**, eaat8127 (2018).
- Maynard, K. R. et al. dotdotdot: an automated approach to quantify multiplex single molecule fluorescent *in situ* hybridization (smFISH) images in complex tissues. *Nucleic Acids Res.* <https://doi.org/10.1093/nar/gkaa312> (2020).
- Burgess, D. J. Spatial transcriptomics coming of age. *Nat. Rev. Genet.* **20**, 317 (2019).
- Lein, E., Borm, L. E. & Linnarsson, S. The promise of spatial transcriptomics for neuroscience in the era of molecular cell typing. *Science* **358**, 64–69 (2017).
- Jaffe, A. E. et al. Profiling gene expression in the human dentate gyrus granule cell layer reveals insights into schizophrenia and its genetic risk. *Nat. Neurosci.* **23**, 510–519 (2020).
- Dong, X. et al. Global, integrated analysis of methylomes and transcriptomes from laser capture microdissected bronchial and alveolar cells in human lung. *Epigenetics* **13**, 264–274 (2018).
- He, Z. et al. Comprehensive transcriptome analysis of neocortical layers in humans, chimpanzees and macaques. *Nat. Neurosci.* **20**, 886–895 (2017).
- Stahl, P. L. et al. Visualization and analysis of gene expression in tissue sections by spatial transcriptomics. *Science* **353**, 78–82 (2016).
- Rodrigues, S. G. et al. Slide-seq: a scalable technology for measuring genome-wide expression at high spatial resolution. *Science* **363**, 1463–1467 (2019).
- Asp, M. et al. An organ-wide gene expression atlas of the developing human heart. *Cell* **179**, 1647–1660.e19 (2019).
- Moncada, R. et al. Integrating microarray-based spatial transcriptomics and single-cell RNA-seq reveals tissue architecture in pancreatic ductal adenocarcinomas. *Nat. Biotechnol.* **38**, 333–342 (2020).
- Berglund, E. et al. Spatial maps of prostate cancer transcriptomes reveal an unexplored landscape of heterogeneity. *Nat. Commun.* **9**, 2419 (2018).
- Maniatis, S. et al. Spatiotemporal dynamics of molecular pathology in amyotrophic lateral sclerosis. *Science* **364**, 89–93 (2019).
- Gregory, J. M. et al. Spatial transcriptomics identifies spatially dysregulated expression of GRM3 and USP47 in amyotrophic lateral sclerosis. *Neuropathol. Appl. Neurobiol.* <https://doi.org/10.1111/nan.12597> (2020).
- Hafner, A.-S., Donlin-Asp, P. G., Leitch, B., Herzog, E. & Schuman, E. M. Local protein synthesis is a ubiquitous feature of neuronal pre- and postsynaptic compartments. *Science* **364**, eaau3644 (2019).
- Molyneaux, B. J., Arlotta, P., Menezes, J. R. L. & Macklis, J. D. Neuronal subtype specification in the cerebral cortex. *Nat. Rev. Neurosci.* **8**, 427–437 (2007).
- Zeng, H. et al. Large-scale cellular-resolution gene profiling in human neocortex reveals species-specific molecular signatures. *Cell* **149**, 483–496 (2012).
- Hawrylycz, M. J. et al. An anatomically comprehensive atlas of the adult human brain transcriptome. *Nature* **489**, 391–399 (2012).
- Birnbaum, R., Jaffe, A. E., Hyde, T. M., Kleinman, J. E. & Weinberger, D. R. Prenatal expression patterns of genes associated with neuropsychiatric disorders. *Am. J. Psychiatry* **171**, 758–767 (2014).
- Abrahams, B. S. et al. SFARI Gene 2.0: a community-driven knowledgebase for the autism spectrum disorders (ASDs). *Mol. Autism* **4**, 36 (2013).
- Satterstrom, F. K. et al. Large-scale exome sequencing study implicates both developmental and functional changes in the neurobiology of autism. *Cell* **180**, 568–584.e23 (2020).
- de Leeuw, C. A., Mooij, J. M., Heskes, T. & Posthuma, D. MAGMA: generalized gene-set analysis of GWAS data. *PLoS Comput. Biol.* **11**, e1004219 (2015).
- Collado-Torres, L. et al. Regional heterogeneity in gene expression, regulation, and coherence in the frontal cortex and hippocampus across development and schizophrenia. *Neuron* **103**, 203–216.e8 (2019).
- Finucane, H. K. et al. Partitioning heritability by functional annotation using genome-wide association summary statistics. *Nat. Genet.* **47**, 1228–1235 (2015).
- Grove, J. et al. Identification of common genetic risk variants for autism spectrum disorder. *Nat. Genet.* **51**, 431–444 (2019).
- Pardiñas, A. F. et al. Common schizophrenia alleles are enriched in mutation-intolerant genes and in regions under strong background selection. *Nat. Genet.* **50**, 381–389 (2018).
- Stahl, E. A. et al. Genome-wide association study identifies 30 loci associated with bipolar disorder. *Nat. Genet.* **51**, 793–803 (2019).

43. Jaffe, A. E. et al. Developmental and genetic regulation of the human cortex transcriptome illuminate schizophrenia pathogenesis. *Nat. Neurosci.* **21**, 1117–1125 (2018).
44. Fromer, M. et al. Gene expression elucidates functional impact of polygenic risk for schizophrenia. *Nat. Neurosci.* **19**, 1442–1453 (2016).
45. Vickovic, S. et al. High-definition spatial transcriptomics for *in situ* tissue profiling. *Nat. Methods* **16**, 987–990 (2019).
46. Chen, K. H., Boettiger, A. N., Moffitt, J. R., Wang, S. & Zhuang, X. RNA imaging. Spatially resolved, highly multiplexed RNA profiling in single cells. *Science* **348**, aaa6090 (2015).
47. Codeluppi, S. et al. Spatial organization of the somatosensory cortex revealed by osmFISH. *Nat. Methods* **15**, 932–935 (2018).
48. Overly, C. C., Rieff, H. I. & Hollenbeck, P. J. Organelle motility and metabolism in axons vs dendrites of cultured hippocampal neurons. *J. Cell Sci.* **109**, 971–980 (1996).
49. Harris, J. J., Jolivet, R. & Attwell, D. Synaptic energy use and supply. *Neuron* **75**, 762–777 (2012).
50. Biever, A., Donlin-Asp, P. G. & Schuman, E. M. Local translation in neuronal processes. *Curr. Opin. Neurobiol.* **57**, 141–148 (2019).

Publisher's note Springer Nature remains neutral with regard to jurisdictional claims in published maps and institutional affiliations.

© The Author(s), under exclusive licence to Springer Nature America, Inc. 2021, corrected publication 2021

Methods

Contact for reagent and resource sharing. Further information and requests for resources and reagents should be directed to and will be fulfilled by the lead contact: A.E.J. (andrew.jaffe@libd.org).

Experimental model and subject details. Postmortem human tissue samples.

Postmortem human brain tissue from three donors of European ancestry (Supplementary Table 1) was obtained by autopsy primarily from the Offices of the Chief Medical Examiner of the District of Columbia and of the Commonwealth of Virginia, Northern District, all with informed consent from the legal next of kin (protocol 90-M-0142 approved by the National Institute of Mental Health (NIMH)/National Institutes of Health (NIH) Institutional Review Board). Clinical characterization, diagnoses, and macro- and microscopic neuropathological examinations were performed on all samples using a standardized paradigm, and subjects with evidence of macro- or microscopic neuropathology were excluded. Details of tissue acquisition, handling, processing, dissection, clinical characterization, diagnoses, neuropathological examinations, RNA extraction and quality control (QC) measures have been described previously⁵¹. Briefly, DLPFC was microdissected and embedded in OCT in a $10 \times 10 \text{ mm}^2$ cryomold. Each sample was dissected in a plane perpendicular to the pial surface in area 46 of the cortex to capture from the pial surface to the gray matter–WM junction, and spanned L1–L6 and the WM.

Method details. Tissue processing and Visium data generation. Frozen samples were embedded in OCT (TissueTek Sakura) and cryosectioned at -10°C (Thermo Cryostar). Sections were placed on chilled Visium Tissue Optimization Slides (catalog no. 3000394, 10x Genomics) and Visium Spatial Gene Expression Slides (catalog no. 2000233, 10x Genomics), and stuck firmly by warming the back of the slide. Tissue sections were then fixed in chilled methanol and stained according to the Visium Spatial Gene Expression User Guide (catalog no. CG000239 Rev A, 10x Genomics) or Visium Spatial Tissue Optimization User Guide (catalog no. CG000238 Rev A, 10x Genomics). For gene expression samples, tissue was permeabilized for 18 min (Supplementary Fig. 1), which was selected as the optimal time based on tissue optimization time-course experiments. Brightfield histology images were taken using a 10 \times objective (Plan APO) on a Nikon Eclipse Ti2-E ($27,755 \times 50,783$ pixels² for TO, $13,332 \times 13,332$ pixels² for GEX). Raw images were stitched together using NIS-Elements AR 5.11.00 (Nikon) and exported as .tiff files with low- and high-resolution settings. For tissue optimization experiments, fluorescent images were taken with a TRITC filter (ex/em brand) using a 10 \times objective and 400-ms exposure time.

Libraries were prepared according to the Visium Spatial Gene Expression User Guide (CG000239: https://assets.ctfassets.net/an68im79xitj/3pyXucRaiKWcscXy3cmRHL/a1ba41c77cbf60366202805ead5f64d7/CG000239_VisiumSpatialGeneExpression_UserGuide_Rev_A.pdf). They were loaded at 300 pM and sequenced on a NovaSeq 6000 System (Illumina) using a NovaSeq S4 Reagent Kit (200 cycles, catalog no. 20027466, Illumina), at a sequencing depth of approximately $250–400 \times 10^6$ read-pairs per sample. Sequencing was performed using the following read protocol: read 1: 28 cycles; i7 index read: 10 cycles; i5 index read: 10 cycles; and read 2: 91 cycles.

Visium raw data processing. Raw FASTQ files and histology images were processed by sample with the Space Ranger software v.1.0.0, which uses STAR v.2.5.1b⁵² for genome alignment, against the Cell Ranger hg38 reference genome refdata-cellranger-GRCh38-3.0.0, available at: <http://cf.10xgenomics.com/supp/cell-exp/refdata-cellranger-GRCh38-3.0.0.tar.gz>. QC metrics returned by this software are available in Supplementary Table 1.

Histology image processing and segmentation. Histology images were processed and nuclei were segmented using the Color-Based Segmentation using K-Means Clustering in Matlab v.R2019a. The Matlab function rgb2lab is used to convert the image from RGB color space to CIELAB color space, also called L*a*b color space (L, luminosity layer measures lightness from black to white; a, chromaticity layer measures color along red–green axis; and b, chromaticity layer measures color along blue–yellow axis). The CIELAB color space quantifies the visual differences caused by the different colors in the image. The a*b color space is extracted from the L*a*b-converted image and is given to the K-means clustering function imsegkmeans, along with the number of colors the user visually identifies in the image. The imsegkmeans outputs a binary mask for each color that it identifies. As the nuclei in the histology images have a bright color that can be easily differentiated from the background, a binary mask generated for the nuclei color is used as the nuclei segmentation.

The segmented binary mask was used to estimate the number of nuclei in each spot. For each histology image, there is a JSON file describing some properties of the image, including the spot diameter in pixels at the full-resolution image. In addition, for each image there is a text file in tabular format that includes one row for each spot with an identification barcode, a row, a column and pixel coordinates for the center of the spot on the full-resolution image. Using this information, the following protocol was implemented: for each spot, all pixels of the binary mask were set to zero except those within the spot radius of the center of that spot. The

resulting binary mask was then labeled with a unique integer for each unique contiguous cluster of pixels. The maximum of this labeled mask was stored as an estimate of the number of nuclei within that spot.

Spot-level data processing. The raw Visium files for each sample (see Visium raw data processing) were read into R in a customized structure using the SummarizedExperiment R package⁵³ to keep them paired with the low-resolution histology images for visualization purposes. They were then combined into a single SingleCellExperiment⁵⁴ v.1.8.0 object (sce) to allow us to perform analyses using the gene-expression data from all samples. We added information, including the number of estimated cell counts (see Histology image processing and segmentation), the sum of UMIs per spot, the number of expressed genes per spot and the graph-based clustering results (computed by sample) provided by 10x Genomics Space Ranger software to the sce object. We evaluated the per-spot quality metrics using the function perCellQCMetrics from the scran v.1.14.3R Bioconductor package⁵⁵ and did not drop any spots given the spatial pattern they presented. We used the scran⁵⁵ functions quickCluster, blocking by the six pairs of spatially adjacent replicates, computeSumFactors and scater's⁵⁶ logNormCounts to compute the log(normalized gene expression counts) at the spot level. By modeling the gene mean expression and variance with the modelGeneVar scran⁵⁵ function, blocking again by the six pairs of spatially adjacent replicates, followed by getTopHVGs, we identified the top 10% HVGs: 1,942 genes. Using this subset of HVGs, we computed principal components (PCs) with scater's v.1.14.3 (ref. ⁵⁶) runPCA to produce 50 components. Using these 50 top PCs, we computed t-distributed stochastic neighbor embedding (t-SNE)⁵⁷ and Uniform Manifold Approximation and Projection (UMAP)⁵⁸ dimension reduction methods using runTSNE (perplexity 5, 20, 50, 80) and runUMAP (15 neighbors) from scater⁵⁶. With the top 50 PCs, we performed graph-based clustering across all samples using 50 nearest neighbors using buildSNNGraph from scran⁵⁵ and the Walktrap method from implemented by igraph⁵⁹ v.1.2.4.1 resulting in 28 clusters (snn_k50_k4 to snn_k50_k28). We further cut the graph to produce clusters from 4 to the 28 in increments of 1. We used spatialLIBD⁶⁰ v.0.99.0 to assign the graph-based clusters from 10x Genomic to the closest anatomical layers for each sample, which was completed by two independent experimenters (K.R.M. and K.M.).

All this information was combined and displayed through a shiny⁶¹ v.1.4.0 web application at <http://spatial.libd.org/spatialLIBD> in such a way that we, and now the scientific community, can visualize the expression of a given gene, or a given set of clustering results, across all samples or each sample individually. For any chosen sample, spatialLIBD allows users to view gene expression and selected cluster results in the context of both spatial histology and given dimension reduction results (principal component analysis (PCA), t-SNE and UMAP) using plotly⁶². Using this web application to visualize cytoarchitecture^{63,64} combined with a dimensionality reduction method, specifically t-SNE⁵⁷, as well as the expression patterns of myelin basic protein (MBP) and PCP4, known WM and L5 marker genes, a single experimenter manually assigned each spot to a cortical layer for each sample for all but 352 out of the 47,681 spots across all samples. These 352 spots were located on small fragments of damaged tissue disconnected from the main tissue section. We added these supervised layer annotations to our sce object and the final version is available for download through the fetch_data function in spatialLIBD⁶⁰.

Layer-level data processing. For the subject with brain ID Br5595, which lacked L1 and clear cytoarchitecture for L2 and L3, we relabeled all L2/L3 ambiguous spots as L3 and dropped the 352 unassigned spots. We then pseudo-bulked^{65–67} the spots into layer-level data by summing the raw gene-expression counts across all spots in a given sample and a given layer, and repeated this procedure for each gene, sample and layer combination (Fig. 2a). This resulted in 47,329 genes quantified across 76 layer-sample combinations ($7 \times 12 = 84$, because not all layers were clearly observed in each sample as Br5595 had no distinct L1 or L2 across all 4 spatial replicates; Supplementary Fig. 5). This resulted in another SingleCellExperiment object called sce_layer. We used librarySizeFactors and logNormCounts from scater⁵⁶ to compute layer-level log(normalized gene expression values). We dropped all mitochondrial genes and retained genes that were expressed in at least 5% (4/76 layer-sample combinations) and had an average count >0.5 as computed by calculateAverage from scater⁵⁶, resulting in a final set of 22,331 genes. We identified 1,280 top HVGs at the layer level and computed 20 PCs (Fig. 2b), which we then used in the t-SNE (perplexity = 5, 15 and 20) and UMAP (15 neighbors) computations. We then clustered the layer-level data using several graph-based approaches as well as k-means. This is the sce_layer data that are available for download through the fetch_data function in spatialLIBD⁶⁰.

Neuropil enrichment analyses. We performed DE analysis at the spot level in our Visium data, comparing the 4,855 spots with 0 cell bodies to the other 42,474 spots containing at least 1 cell body, adjusting for fixed effects of layer and spatial replicate. We downloaded DE statistics from RNA-seq of vGLUT1⁺-enriched synaptosomes in mouse brain from Hafner et al.³⁰, and lined up these data at the gene level using homologous Entrez IDs between mouse and human (via http://www.informatics.jax.org/downloads/reports/HMD_HumanPhenotype.rpt). We compared the effects of spots containing 0 cells in our data with

vGLUT1⁺-enriched cells from Hafner et al., both across the full homologous transcript and then within genes significant in the Hafner dataset at FDR < 0.05.

Layer-level gene modeling. Using the layer-level data we fit three types of models (Fig. 2c and Extended Data Fig. 4):

1. ANOVA: for this model we tested for each gene whether the log(normalized gene expression counts) are variable between the layers by computing *F* statistics. We used lmFit and eBayes from limma⁶⁸ v.3.42.0 after blocking by the six pairs of spatially adjacent replicates and taking this correlation into account as computed by duplicateCorrelation.
2. Enrichment: using the same functions and taking into account the same correlation structure, we computed Student's *t*-test statistics comparing one layer against the other six using the layer-level data. This resulted in seven sets of Student's *t*-test statistics (one per layer) with double-sided *P* values. We focused on genes with positive Student's *t*-test statistics (expressed higher in one layer against the others) because these are enriched genes rather than depleted genes.
3. Pairwise: using the same functions and taking into account the same correlation structure in addition to using contrasts.fit from limma⁶⁸, we computed the Student's *t*-test statistics for each pair of layers resulting in Student's *t*-test statistics with double-sided *P* values.

The modeling results are available for download through the fetch_data function in spatialLIBD⁶⁰ as the modeling_results object as well as in Supplementary Table 4.

Known marker gene optimal modeling. Using two lists of known layer-marker genes derived from previous mouse or human studies^{31,32}, we identified 29 different unique optimal models for these genes, for example, L1 + L2 versus the other layers. Using the same modeling framework (see Layer-level data processing) we computed Student's *t*-test statistics for all genes at the layer-level data for each of these 29 unique models. For each of the 29 unique models, we then retained information about the statistics for the known marker genes matching the model, as well as the top ranked ones (with a positive Student's *t*-test statistic gene; Supplementary Table 5).

RNAscope smFISH. Fresh frozen DLPFC from the same three neurotypical control samples used for Visium were sectioned at 10 µm and stored at -80°C. ISH assays were performed with RNAscope technology utilizing the RNAscope Fluorescent Multiplex Kit v.2 and 4-plex Ancillary Kit (catalog no. 323100, 323120 ACD) according to the manufacturer's instructions. Briefly, tissue sections (two to four per individual) were fixed with a 10% neutral buffered formalin solution (catalog no. HT501128, Sigma-Aldrich) for 30 min at room temperature, series dehydrated in ethanol, pretreated with hydrogen peroxide for 10 min at room temperature and treated with protease IV for 30 min. Sections were incubated with four different probe combinations: (1) L1 and L5: *AQP4*, *RELN*, *TRABD2A* and *BCL11B* (catalog nos. 482441-C4, 413051-C2, 532881 and 425561-C3, ACD); (2) L3 and L6: *CARTPT*, *FREM3* and *NR4A2* (catalog nos. 506591, 829021-C4 and 582621-C3); (3) L2/3 and WM: *LAMP5*, *HPCAL1*, *NDRG1* and *MBP* (catalog nos. 487691-C2, 846051-C3, 481471 and 411051-C4); and (4) Visium-identified genes: *AQP4*, *TRABD2A*, *KRT17* (catalog no. 463661-C2) and *HPCAL1*. After probe labeling, sections were stored overnight in 4× saline-sodium citrate buffer. After amplification steps (AMP1-3), probes were fluorescently labeled with Opal Dyes (Perkin Elmer; 1:500) and stained with DAPI (4',6-diamidino-2-phenylindole) to label the nucleus. Lambda stacks were acquired in z-series using a Zeiss LSM780 confocal microscope equipped with 20×, 1.4 numerical aperture (NA) and 63×, 1.4 NA objectives, a GaAsP spectral detector, and 405-, 488-, 555- and 647-nm lasers. All lambda stacks were acquired with the same imaging settings and laser power intensities. For each subject, a cortical strip was tile imaged at 20× to capture L1 to WM. After image acquisition, lambda stacks in z-series were linearly unmixed using Zen Black (weighted; no autoscale) using reference emission spectral profiles previously created in Zen for dotdotdot (git hash v.4e1350b)⁷⁷, stitched, maximum intensity projected and saved as Carl Zeiss Image 'czi' files.

snRNA-seq spatial registration. For each snRNA-seq dataset, we utilized publicly available, processed UMI count data for each gene and nucleus, and provided annotations of cell clusters/subtypes. Within each dataset, we performed pseudo-bulking^{65–67} of nuclei-level UMIs into cell type-specific log(transformed normalized counts) for each unique subject. We then computed cell-type enrichment statistics for each gene and dataset-provided cell type within their pseudo-bulk profiles by performing linear mixed effects modeling, comparing each cell type to all other cell types, treating a donor as a random intercept⁶⁸, and adjusting for the study-specific covariates described below. This strategy was analogous to the layer enrichment statistics described for our Visium data. We then computed Pearson's correlation coefficients between our layer-enriched and our snRNA-seq cell-type-specific enrichment statistics among the 700 most layer-enriched genes (combining the 100 most significant genes for each of the six layers and WM in the Visium data), expressed in each snRNA-seq dataset. In addition to our DLPFC snRNA-seq dataset, we utilized these publicly available datasets:

1. Hodge et al.⁵: processed data were obtained from <https://portal.brain-map.org/atlas-and-data/rnaseq>. We retained total gene counts (exons plus introns) from 49,494 nuclei corresponding to postmortem human brain tissue across both neurons and non-neurons with 50,281 genes, 6 layers and 2 cell types. These data were reduced to 52 pseudo-bulk profiles, for all unique donor-layer-type combinations. We calculated enrichment statistics for each of the six layers in their dataset, adjusting for the fixed effect of cell type (neuronal or glial) with a random intercept of donor.
2. Velmeshev et al.⁶: processed data were obtained from <https://cells.ucsc.edu> (under the 'Autism' study data download option). We used the post-QC UMI counts from all 104,559 nuclei across 65,217 genes with 41 unique donor-region pairs (for 31 unique donors and 2 brain regions) and 17 cell types. These data were reduced to 691 pseudo-bulked profiles, for all unique donor-region-type combinations. We calculated enrichment statistics for each of the 17 cell types in this dataset, adjusting for the fixed effect of brain region, age, sex and ASD diagnosis, with a random intercept of donor.
3. Mathys et al.¹⁰: processed data were obtained from Synapse at accession no. syn18485175. We used the post-QC UMI counts from all 70,634 nuclei across 17,926 genes of 48 unique donors and 44 cell subtypes (across 8 broad cell classes). These data were reduced to 1,877 pseudo-bulked profiles, for all unique donor-subtype combinations. We calculated enrichment statistics for each of the 44 cell subtypes in this dataset, adjusting for the fixed effect of age, sex, race and Alzheimer's disease diagnosis, with a random intercept of donor.
4. We also downloaded and reprocessed RNA-seq data from He et al.²² from Sequence Read Archive (SRA) accession no. SRP199498 using our previously described RNA-seq processing pipeline³⁸. These data consisted of homogenate RNA-seq data from 18 serial sections across 4 unique donors.

DLPFC snRNA-seq data generation. We performed snRNA-seq on DLPFC tissue from two neurotypical donors using 10x Genomics Chromium Single Cell Gene Expression v.3 technology. Nuclei were isolated using a 10x Genomics customer-developed Frankenstein nuclei isolation protocol developed by Martelotto et al. (<https://www.10xgenomics.com/resources/customer-developed-protocols>) for frozen tissues^{8,70–73}. Briefly, ~40 mg of frozen DLPFC tissue was homogenized in chilled Nuclei EZ Lysis Buffer (MilliporeSigma) using a glass dounce with ~15 strokes per pestle. Homogenate was filtered using a 70-µm-strainer mesh and centrifuged at 500g for 5 min at 4°C in a benchtop centrifuge. Nuclei were resuspended in the EZ lysis buffer, centrifuged again and equilibrated to nuclei wash/resuspension buffer (1× phosphate-buffered saline, 1% bovine serum albumin, 0.2 U µl⁻¹ of RNase Inhibitor). Nuclei were washed and centrifuged in this nuclei wash/resuspension buffer three times, before labeling with DAPI (10 µg ml⁻¹). The sample was then filtered through a 35-µm cell strainer and sorted on a BD FACS Aria II Flow Cytometer (Becton Dickinson) at the Johns Hopkins University Sidney Kimmel Comprehensive Cancer Center (SKCCC) Flow Cytometry Core into 10x Genomics reverse transcription reagents. Gating criteria were hierarchically selected for whole, singlet nuclei (by forward/side scatter), then for G0/G1 nuclei (by DAPI fluorescence). A null sort into wash buffer was additionally performed from the same preparation for quantification of nuclei concentration and to ensure nuclei input was free of debris. Approximately 8,500 single nuclei were sorted directly into 25.1 µl of reverse transcription reagents from the 10x Genomics Single Cell 3' Reagents kit (without enzyme). Libraries were prepared according to the manufacturer's instructions (10x Genomics) and sequenced on the Next-seq (Illumina) at the Johns Hopkins University Transcriptomics and Deep Sequencing Core.

We processed the sequencing data with the 10x Genomics' Cell Ranger pipeline v.3.0.2, aligning to the human reference genome GRCh38, with a reconfigured Gene transfer format such that intronic alignments were also counted given the nuclear context, to generate UMI/feature-barcode matrices (<https://support.10xgenomics.com/single-cell-gene-expression/software/pipelines/latest/advanced/references>). We started with raw feature-barcode matrices for analysis with the Bioconductor suite of R packages for scRNA-seq analysis⁴. For QC and cell calling, we first used a Monte Carlo simulation-based approach to assess and rule out empty droplets or those with random ambient transcriptional noise, such as from debris^{75,76}. This was then followed by mitochondrial rate-adaptive thresholding, which, although expected to be near zero in this nuclear context, we allowed for a three times median absolute deviation threshold. This allowed for flexibility in output/purity of FACS workflows. This QC pipeline yielded 5,399 high-quality nuclei from the DLPFC of two donors, which were rescaled across all nuclear libraries and then log(transformed) for determination of HVGs, again with scan's modelGeneVar, this time taking all genes (9,313) with a greater variance than the fitted trend. PCA was then performed on these selected genes to reduce the high dimensionality of nuclear transcriptomic data. The optimal PC space was defined with iterative graph-based clustering to determine the *d*PCs where resulting *n* clusters stabilize, with the constraint that *n* clusters <= (*d*+1) PCs⁵⁵, resulting in a chosen *d*=81 PCs. In this PCA-reduced space, graph-based clustering was performed (specifically, *k*-nearest neighbors with *k*=20 neighbors and the Walktrap method from R package igraph⁵⁹ for community detection) to identify 31 preliminary clusters. We then took all feature counts for these assignments and pseudo-bulked counts across 31 preliminary nuclear clusters, rescaling for

combined library size and log(transferring normalized counts), and then we performed hierarchical clustering to identify preliminary cluster relationships and merge with the cutreeDynamic function of R package dynamicTreeCut⁷⁷ v1.63.1. These broader clusters were finally annotated with well-established cell-type markers for nuclear-type identity¹⁰. We also used Bioconductor package scater's⁵⁶ implementation of nonlinear dimensionality reduction techniques, t-SNE and UMAP, with default parameters and within the aforementioned optimal PC space, simply for visualization of the high-dimensional structure in the data, which complemented the clustering results (Supplementary Fig. 9).

Clinical gene set enrichment analyses. We assessed the laminar enrichment of a series of predefined clinical gene sets for various neuropsychiatric and neurodevelopmental disorders. These gene sets consisted of data from:

1. Birnbaum et al.³⁴: ten gene sets across SCZ, ASD, neurodevelopmental delays, intellectual disability, BPD and neurodegenerative disorders
2. SFARI³⁵: three gene sets consisting of all human genes, high confidence genes and syndromic genes
3. Satterstrom et al.³⁶: six gene sets based on exome sequencing studies
4. psychENCODE¹⁶: six gene sets based on DE analyses of patients with ASD, SCZD and BPD, stratified by directionality in cases, and eight gene sets based on TWAS⁷⁸ (ASD, SCZD, BPD, SCZD–BPD, stratified by directionality), each at FDR < 0.05
5. BrainSeq³⁸: two gene sets based on DE analyses of patients with SCZD versus controls (at FDR < 0.05), stratified by directionality
6. Down's syndrome⁷⁹: two gene sets based on DE analyses of patients with Down's syndrome versus controls (at FDR < 0.05), stratified by directionality

We collected all reported genes in each gene set, and retained the majority that were expressed in our Visium dataset—these gene set sizes are provided in Supplementary Table 6. Enrichment for each gene set for each layer was based on a gene being significantly more highly expressed in one layer versus all other layers (at FDR < 0.1, because this cutoff for defining genes with increased expression was approximately as conservative as using an FDR < 0.05 cutoff with either direction). This calculation was performed using Fisher's exact test, which returned an OR and P value for each gene set and layer (Supplementary Table 6). Pooling all P values resulted in FDR control of 5% for marginal P values < 0.01.

We additionally performed MAGMA⁷ v.1.07b using the subset of 24,347 Ensembl gene IDs expressed in our pseudo-bulked Visium data that were present in the provided GR37/hg19 annotation across multiple GWASs for SCZD⁴¹, BPD⁴², major depressive disorder⁸⁰ and ASD⁴⁰. We used window sizes of +35 kb and -10 kb around each gene to aggregate SNPs to genes using the 1000 Genomes EUR reference profile with SNP-wise stats. We then performed gene-set testing using MAGMA for seven gene sets (related to the six layers and WM) for genes with positive enrichment statistics at FDR < 0.1. In addition, we performed linkage disequilibrium score regression (LDSC v.1.0.1) and partitioned heritability analysis^{39,81} using 30 GWAS traits collected by Rizzardi et al.⁸². Genomic regions were created from the same enriched and FDR < 0.1 genes as above, here with +10 kb and -5 kb windows, and lifted over to hg19 coordinates.

Data-driven, layer-enriched clustering analysis. For the data-driven, layer-enriched clustering, we first performed feature selection in two ways to identify laminar and nonlaminar patterns in our data. The first method for feature selection used was SpatialDE⁸³ to identify genes exhibiting SVGs. SpatialDE was run in Python v.3.8.0. We ran SpatialDE individually on each of the 12 samples, which returned a set of statistically significant (FDR < 0.05) SVGs per sample. We included an additional filtering step to remove lowly expressed genes (<1,000 total UMIs summed across spots per sample), as well as removing mitochondrial genes. This left between 521 and 2,217 genes per sample (Supplementary Table 9). In total, there were 2,775 unique genes across samples; for comparison, we also ran clustering methods using this pooled list (Supplementary Tables 9 and 10). The second feature selection method used the scran R Bioconductor package⁵⁵ to identify (nonspatial) HVGs across all samples combined, which identified 1,942 HVGs. Due to slow runtime, it was not possible to run SpatialDE on pooled spots from all samples combined.

In the unsupervised approach to define subgroups of spots with similar expression profiles in a completely data-driven manner, we considered the possible combinations of: (1) two types of methods for dimensionality reduction (top 50 PCs with the BiocSingular v.1.2.2 Bioconductor package⁸⁴ and top 10 UMAP⁵⁸ components with the uwot v.0.1.5 R package⁸⁵ calculated on the top 50 PCs); (2) the gene sets defined after applying feature selection (SpatialDE genes for each sample, pooled SpatialDE gene lists across all 12 samples and HVGs); and (3) including (or not) the two spatial coordinates (x and y coordinates) of each spot as additional features for clustering. For the clustering algorithm, we constructed a shared nearest-neighbor graph with the scran Bioconductor package and then applied the Walktrap method from the igraph R package⁸⁶ to obtain predicted cluster labels. We set all clustering implementations to return eight final clusters (that is, one more than the six DLPFC layers plus WM), which gave slightly improved clustering performance (compared with seven clusters) due to additional splitting of the WM cluster and some outlier spots. Supplementary Table 10 contains an overview of all combinations that were tried.

For comparison, we also implemented a semi-supervised approach, in which we used the layer-enriched gene sets identified using the DE enrichment models described previously (Extended Data Fig. 4) and a markers approach using known marker genes from Zeng et al.³² (Supplementary Table 10).

To evaluate the performance of the clustering approaches, we used the ARI, which measures the similarity between the predicted cluster labels and gold standard cluster labels. The manually annotated layers were used as the gold standard (Fig. 7 and Supplementary Fig. 11). Higher ARI values correspond to better clustering performance, with a maximum value of 1 indicating perfect clustering agreement. To evaluate the improvement in ARI when including spatial coordinates within the clustering methods, we fit a linear model on the ARI scores, comparing these methods against methods without spatial coordinates across all methods and samples, and recorded the P value.

The link https://github.com/LieberInstitute/HumanPilot/blob/master/Analysis/Layer_Guesses/pdf/SFileXX_clustering_compressed.pdf contains visualizations of clustering results for all samples and clustering methods (Supplementary Table 10) (similar to Extended Data Figs. 9 and 10, which display results for sample 151673 only). A description of the clustering methods is provided in Supplementary Table 10.

Statistics and reproducibility. No statistical methods were used to predetermine sample sizes, but our sample sizes are greater than those cited in previous publications with the earlier spatial transcriptomics technology that preceded Visium^{23,28}. Supplementary Table 1 contains the demographic information (two males, one female, neurotypical controls with age at time of death from 30 years to 46 years) for the three donor brains we used to generate the six pairs of spatial replicates (two per donor) for a total of twelve images. All boxplots shown in the main and supplementary figures displayed the median as the center, IQR (25th and 75th percentiles) as the box ranges, and 1.5× the IQR as the whiskers. All reported P values were two sized and all P values were adjusted for multiple testing with the Benjamini–Hochberg correction unless otherwise indicated. Distributions of the residuals of our many linear models were assumed to be normally distributed across all genes and models, but this was not formally tested. All points were used in all analyses, for example, outliers were not removed. We used the six pairs of spatial replicates as a blocking factor in our analyses. Data collection and analysis were not performed blind to the conditions of the experiments. See the Nature Research Reporting Summary for further details.

Quantification and statistical analyses. The different subsections under Method details further specify the statistical models and tests used as well as the versions of the specific software used. Overall, statistical tests were performed using R v.3.6.1 and v.3.6.2 with Bioconductor v.3.10 with detailed R session information provided in the code GitHub repositories listed below. The threshold and method used for statistical significance are listed in the main text along with the description of the results. Plots in R were created either in base R or with the ggplot2 R package⁸⁶.

Additional resources. To visualize the spot-level Visium data that we generated, we created a shiny⁶¹ interactive browser available at <http://spatial.libd.org/spatialLIBD> which is powered by the Bioconductor package spatialLIBD⁶⁰.

Reporting Summary. Further information on research design is available in the Nature Research Reporting Summary linked to this article.

Data availability

Processed data are publicly available from the Bioconductor package spatialLIBD⁶⁰. The raw data are publicly available from the Globus endpoint 'jhpc@HumanPilot10x' that is also listed at <http://research.libd.org/globus>. The raw data provided through Globus include all the FASTQ files and raw image files. External data used in this project are detailed under snRNA-seq spatial registration as well as Clinical gene set enrichment analyses.

Code availability

The code for this project is publicly available through GitHub and archived through Zenodo. Specifically, the code is available through GitHub at <https://github.com/LieberInstitute/HumanPilot> (ref. ⁸⁷) and <https://github.com/LieberInstitute/spatialLIBD> (ref. ⁶⁰), both of which are described in their README.md files.

References

51. Lipska, B. K. et al. Critical factors in gene expression in postmortem human brain: focus on studies in schizophrenia. *Biol. Psychiatry* **60**, 650–658 (2006).
52. Dobin, A. et al. STAR: ultrafast universal RNA-seq aligner. *Bioinformatics* **29**, 15–21 (2013).
53. Morgan, M., Obenchain, V., Hester, J. & Pagès, H. Summarized Experiment. *Bioconductor* <https://doi.org/10.18129/b9.bioc.summarizedexperiment> (2017).
54. Risso, D. Single cell experiment. *Bioconductor* <https://doi.org/10.18129/b9.bioc.singlecellexperiment> (2017).
55. Lun, A. T. L., McCarthy, D. J. & Marioni, J. C. A step-by-step workflow for low-level analysis of single-cell RNA-seq data with bioconductor. *F1000Res.* **5**, 2122 (2016).

56. McCarthy, D. J., Campbell, K. R., Lun, A. T. L. & Wills, Q. F. Scater: pre-processing, quality control, normalization and visualization of single-cell RNA-seq data in R. *Bioinformatics* **33**, 1179–1186 (2017).
57. van der Maaten, L. & Hinton, G. Visualizing data using t-SNE. *J. Mach. Learn. Res.* **9**, 2579–2605 (2008).
58. McInnes, L., Healy, J., Saul, N. & Großberger, L. UMAP: uniform manifold approximation and projection. *J. Open Source Software* **3**, 861 (2018).
59. Csardi, G. & Nepusz, T. The igraph software package for complex network research. *InterJournal, Complex Syst.* **1695**, 1–9 (2006).
60. Collado-Torres, L. LieberInstitute/spatialLIBD: spatialLIBD: initial bioconductor submission. *Zenodo* <https://doi.org/10.5281/zenodo.3689719> (2020).
61. Chang, W., Cheng, J., Allaire, J. J., Xie, Y. & McPherson, J. shiny: Web application framework for R. R version 1.4.0 (2019).
62. Sievert, C. plotly for R. R version 4.9.2 (2018).
63. Rajkowska, G. & Goldman-Rakic, P. S. Cytarchitectonic definition of prefrontal areas in the normal human cortex: I. Remapping of areas 9 and 46 using quantitative criteria. *Cereb. Cortex* **5**, 307–322 (1995).
64. Rajkowska, G. & Goldman-Rakic, P. S. Cytarchitectonic definition of prefrontal areas in the normal human cortex: II. Variability in locations of areas 9 and 46 and relationship to the Talairach coordinate system. *Cereb. Cortex* **5**, 323–337 (1995).
65. Lun, A. T. L. & Marioni, J. C. Overcoming confounding plate effects in differential expression analyses of single-cell RNA-seq data. *Biostatistics* **18**, 451–464 (2017).
66. Kang, H. M. et al. Multiplexed droplet single-cell RNA-sequencing using natural genetic variation. *Nat. Biotechnol.* **36**, 89–94 (2018).
67. Crowell, H. L. et al. muscat detects subpopulation-specific state transitions from multi-sample multi-condition single-cell transcriptomics data. *Nat. Commun.* **11**, 6077 (2020).
68. Ritchie, M. E. et al. limma powers differential expression analyses for RNA-sequencing and microarray studies. *Nucleic Acids Res.* **43**, e47 (2015).
69. Law, C. W., Chen, Y., Shi, W. & Smyth, G. K. voom: precision weights unlock linear model analysis tools for RNA-seq read counts. *Genome Biol.* **15**, R29 (2014).
70. Habib, N. et al. Massively parallel single-nucleus RNA-seq with DroNc-seq. *Nat. Methods* **14**, 955–958 (2017).
71. Lacar, B. et al. Nuclear RNA-seq of single neurons reveals molecular signatures of activation. *Nat. Commun.* **7**, 11022 (2016).
72. Habib, N. et al. Div-Seq: single-nucleus RNA-Seq reveals dynamics of rare adult newborn neurons. *Science* **353**, 925–928 (2016).
73. Hu, P. et al. Dissecting cell-type composition and activity-dependent transcriptional state in mammalian brains by massively parallel single-nucleus RNA-Seq. *Mol. Cell* **68**, 1006–1015.e7 (2017).
74. Amezquita, R. A. et al. Orchestrating single-cell analysis with bioconductor. *Nat. Methods* **17**, 137–145 (2020).
75. Lun, A. T. L. et al. EmptyDrops: distinguishing cells from empty droplets in droplet-based single-cell RNA sequencing data. *Genome Biol.* **20**, 63 (2019).
76. Griffiths, J. A., Richard, A. C., Bach, K., Lun, A. T. L. & Marioni, J. C. Detection and removal of barcode swapping in single-cell RNA-seq data. *Nat. Commun.* **9**, 2667 (2018).
77. Langfelder, P., Zhang, B. & with contributions from Horvath, S. dynamicTreeCut: Methods for detection of clusters in hierarchical clustering dendograms. R version 1.63.1 (2016).
78. Gusev, A. et al. Integrative approaches for large-scale transcriptome-wide association studies. *Nat. Genet.* **48**, 245–252 (2016).
79. Olmos-Serrano, J. L. et al. Down syndrome developmental brain transcriptome reveals defective oligodendrocyte differentiation and myelination. *Neuron* **89**, 1208–1222 (2016).
80. Wray, N. R. et al. Genome-wide association analyses identify 44 risk variants and refine the genetic architecture of major depression. *Nat. Genet.* **50**, 668–681 (2018).
81. Bulik-Sullivan, B. et al. LD Score regression distinguishes confounding from polygenicity in genome-wide association studies. *Nat. Genet.* **47**, 291–295 (2015).
82. Rizzardi, L. F. et al. Neuronal brain-region-specific DNA methylation and chromatin accessibility are associated with neuropsychiatric trait heritability. *Nat. Neurosci.* **22**, 307–316 (2019).
83. Svensson, V., Teichmann, S. A. & Stegle, O. SpatialDE: identification of spatially variable genes. *Nat. Methods* **15**, 343–346 (2018).
84. Lun, A. BioS Singular. *Bioconductor* <https://doi.org/10.18129/b9.bioc.biocsingular> (2019).
85. Melville, J. uwot: R package. R version 0.1.5 (2019).
86. Wickham, H. *ggplot2—Elegant Graphics For Data Analysis* <https://doi.org/10.1007/978-3-319-24277-4> (Springer, 2016).
87. Collado-Torres, L., Weber, L. & Hicks, S. LieberInstitute/HumanPilot: archive the HumanPilot code for the preprint version of our project. *Zenodo* <https://doi.org/10.5281/zenodo.3691916> (2020).

Acknowledgements

We thank our colleagues whose efforts have led to the donation of postmortem tissue to advance these studies, including at the Office of the Chief Medical Examiner of the State of Maryland, Baltimore, MA and the Office of the Chief Medical Examiner of Kalamazoo County, Michigan. We also thank L. B. Bigelow and A. Deep-Soboslay for their contributions of diagnostic expertise, and D. R. Weinberger for providing constructive commentary and editing of the manuscript. Finally, we thank the families of the decedents, who donated the brain tissue used in these studies. We also thank the Accelerating Medicines Partnership—Alzheimer’s Disease (AMP-AD) Target Discovery and Preclinical Validation program and the ROSMAP study. We thank W. S. Ulrich for assistance with <http://spatial.libd.org/spatialDE> and the Department of Biostatistics at the Johns Hopkins Bloomberg School of Public Health for hosting mirrors of our web application. We thank the Johns Hopkins University SKCCC Flow Cytometry Core and the Johns Hopkins University Transcriptomics and Deep Sequencing Core for supporting snRNA-seq experiments. This project was supported by the Lieber Institute for Brain Development. K.R.M., L.C.-T., K.M. and A.E.J. were partially supported by the NIMH (grant no. U01MH122849). S.C.H. and L.M.W. were supported by the National Cancer Institute (grant no. R01CA237170). S.C.H. was also supported by the CZF2019-002443 from the Chan Zuckerberg Initiative DAF, an advised fund of Silicon Valley Community Foundation, the National Human Genome Research Institute (grant no. R00HG009007).

Author contributions

K.R.M. carried out conceptualization, methodology, validation, investigation, writing and visualization. L.C.-T. dealt with methodology, software, formal analysis, data curation, writing and visualization. L.M.W. dealt with methodology, software, formal analysis, writing and visualization. C.U. dealt with methodology, investigation and resources. B.K.B. dealt with formal analysis, data curation and visualization. S.R.W. dealt with software and data curation. J.L.C. dealt with software, formal analysis and visualization. M.N.T. dealt with investigation and formal analysis. Z.B. dealt with software. M.T. dealt with formal analysis and visualization. J.C. and Y.Y. dealt with investigation. J.E.K. dealt with resources. T.M.H. dealt with methodology and resources. N.R. dealt with resources, supervision and funding acquisition. S.C.H. dealt with methodology, software, formal analysis, writing, visualization and supervision. K.M. dealt with conceptualization, methodology, writing, supervision, project administration and funding acquisition. A.E.J. dealt with conceptualization, methodology, software, formal analysis, writing, visualization, supervision, project administration and funding acquisition.

Competing interests

C.U., S.R.W., J.C., Y.Y. and N.R. are employees of 10x Genomics. All other authors declare no conflicts of interest.

Additional information

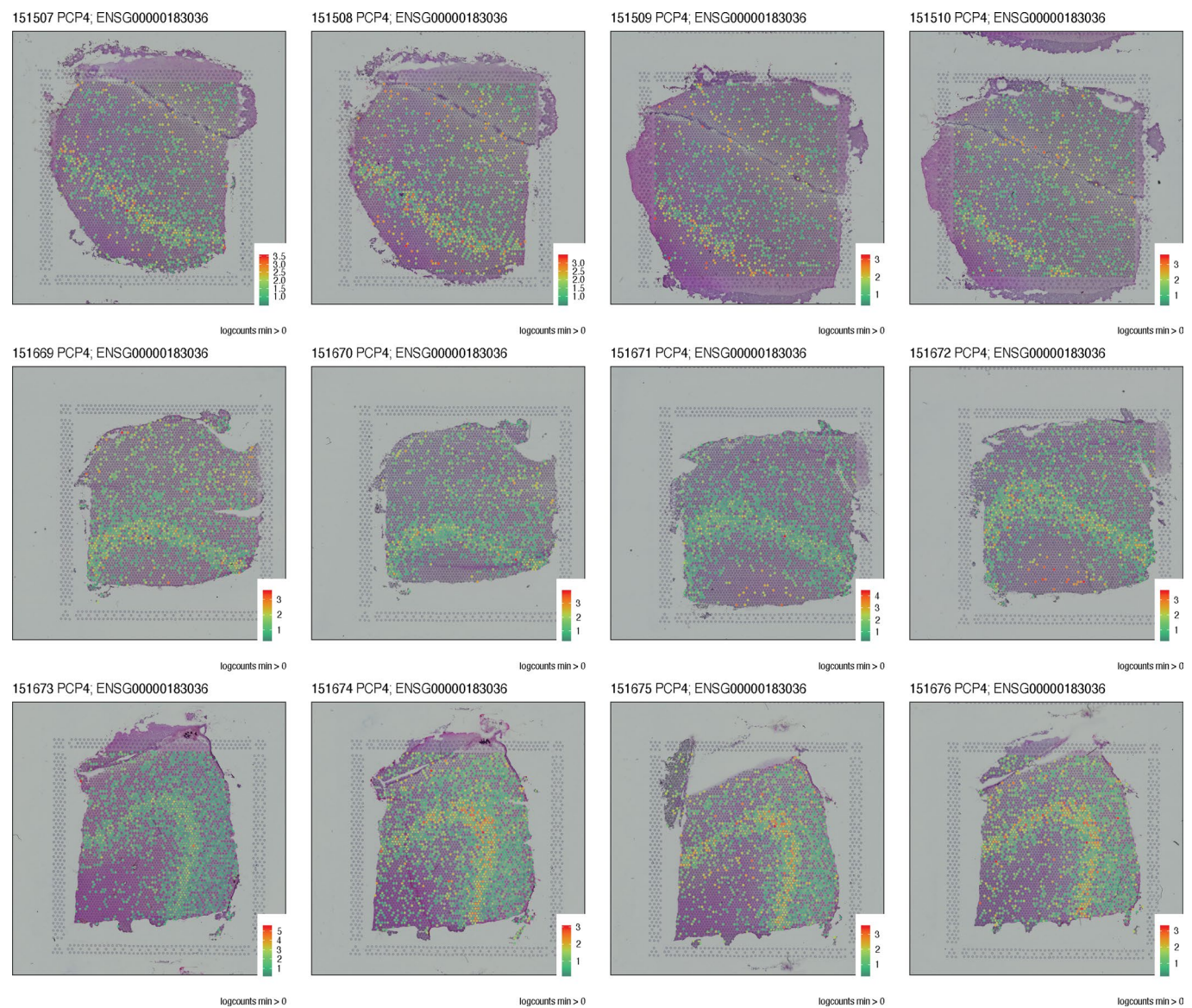
Extended data is available for this paper at <https://doi.org/10.1038/s41593-020-00787-0>.

Supplementary information The online version contains supplementary material available at <https://doi.org/10.1038/s41593-020-00787-0>.

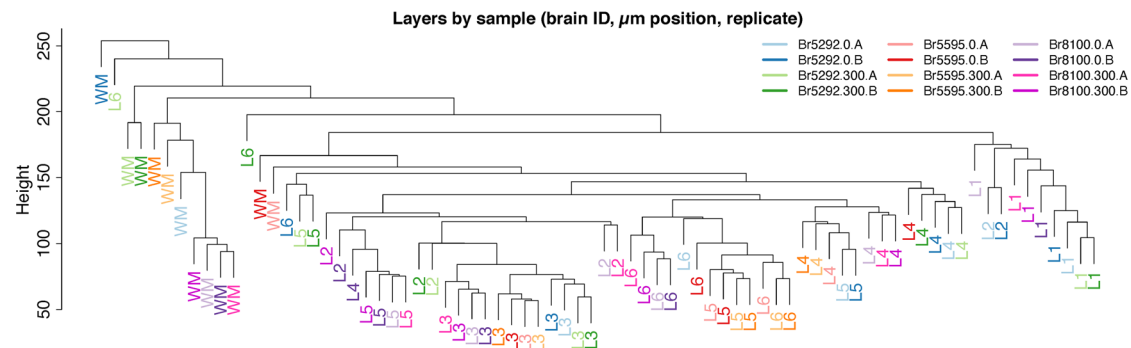
Correspondence and requests for materials should be addressed to K.M. or A.E.J.

Peer review information *Nature Neuroscience* thanks the anonymous reviewers for their contribution to the peer review of this work.

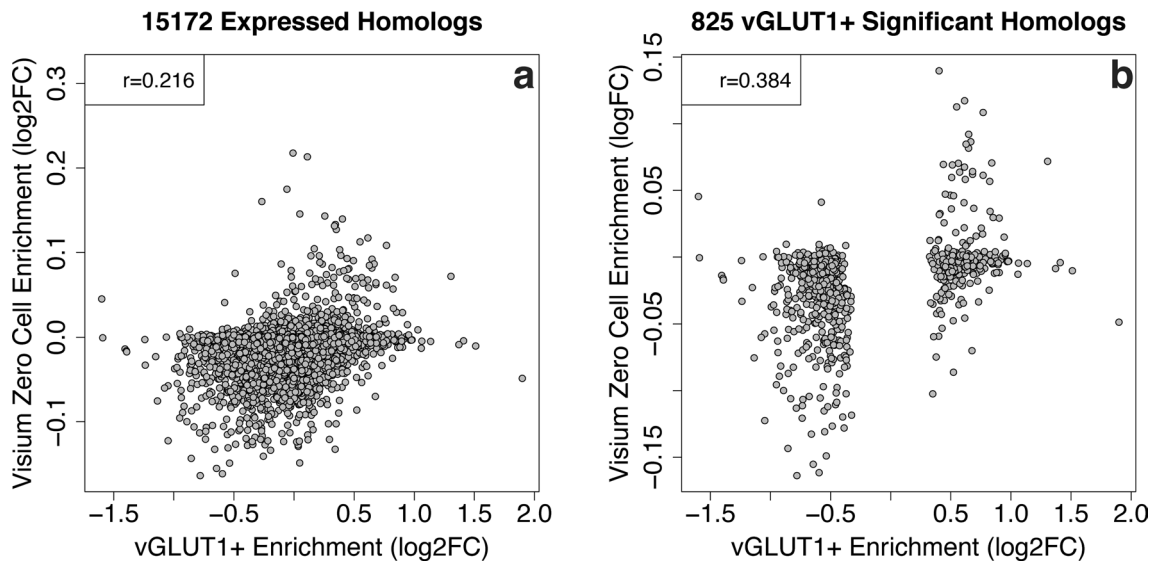
Reprints and permissions information is available at www.nature.com/reprints.



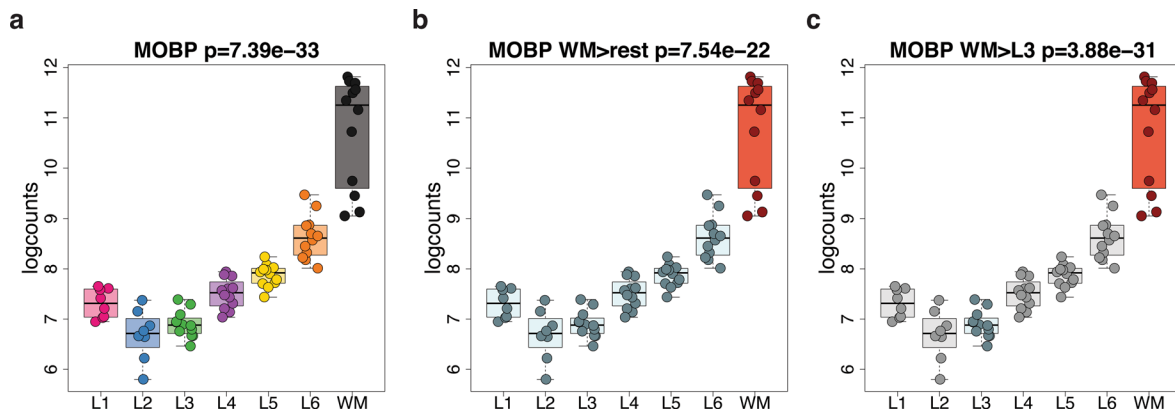
Extended Data Fig. 1 | PCP4 expression, related to Fig. 1f. Log-transformed normalized (logcounts) for PCP4 gene expression across all 12 samples arranged in rows by subject.



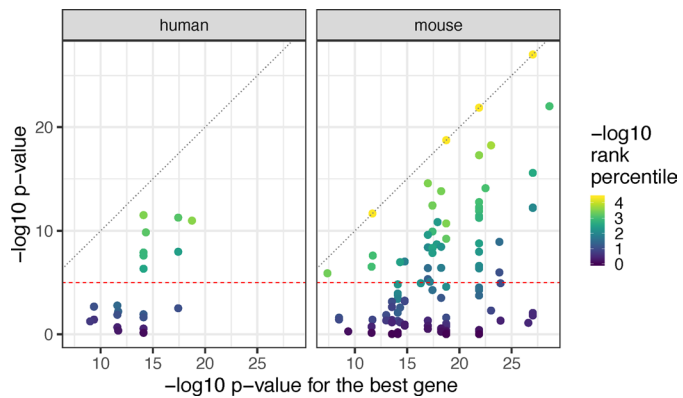
Extended Data Fig. 2 | Layer-level dendrogram, related to Results: Gene expression in the DLPFC across cortical laminae and Fig. 2. Dendrogram from the hierarchical clustering performed across all 76 layer-level combinations: 6 layers plus WM across 12 samples, with two layers visually absent in one sample as shown in Supplementary Fig. 5, second row. The layer-level combinations are colored by the brain subject (BR5292, Br5595, Br8100), position (0 or 300) and adjacent spatial replicate number (A or B).



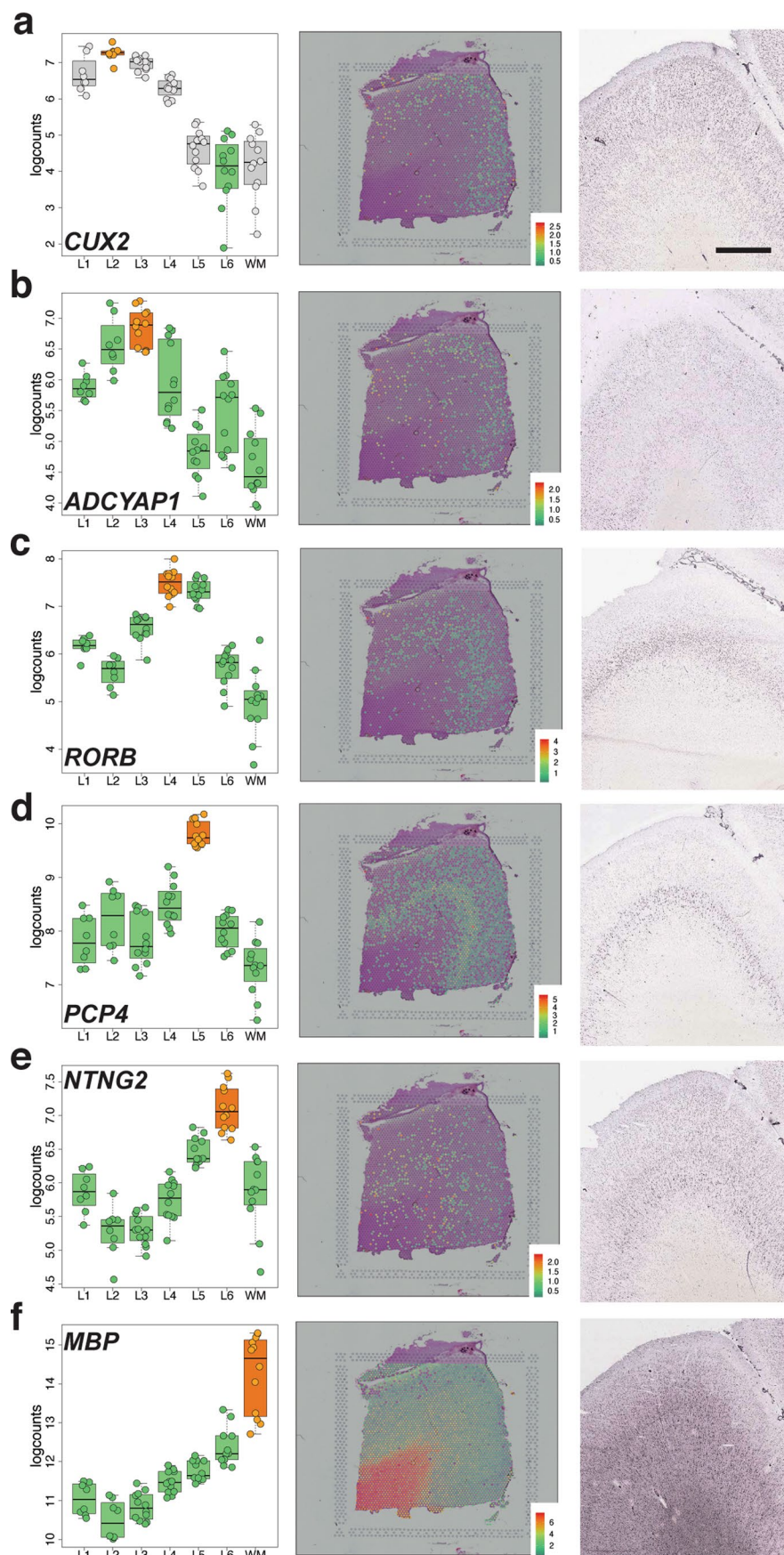
Extended Data Fig. 3 | Enrichment of genes expressed in synaptic terminals among neuropil spots, related to Results: Gene expression in the DLPFC across cortical laminae. We compared DEGs from VGLUT1+ labeled synaptosomes from mouse brain from Hafner *et al.*³⁰ on the x-axis versus the log₂ fold change comparing spot-level expression between spots with 0 cells and spots with >0 cells. Association shown between (a) all expressed homologous genes and (b) those genes that were significant in the Hafner *et al.* dataset at FDR < 0.05.



Extended Data Fig. 4 | Layer-level modeling strategies illustrated with MOBP, related to Results: Fig. 2. Overview of the different modeling strategies we performed with the layer-level pseudo-bulked expression data. **a**, The ANOVA model, which evaluates whether the gene is variable in any of the layers (F-statistic); MOBP is the top 10th ranked of such genes. Colors represent each layer. **b**, The enrichment model, which tests one layer against the rest (t-statistic); MOBP is the top 36th gene for white matter against other layers. Colors show the comparison being done. **c**, The pairwise model where we test one layer against another (t-statistic); MOBP is the top ranked gene for WM > L3. Data from layers not used is shown in gray. 76 pseudo-bulked layers were used for computing the statistics in **a–c**.

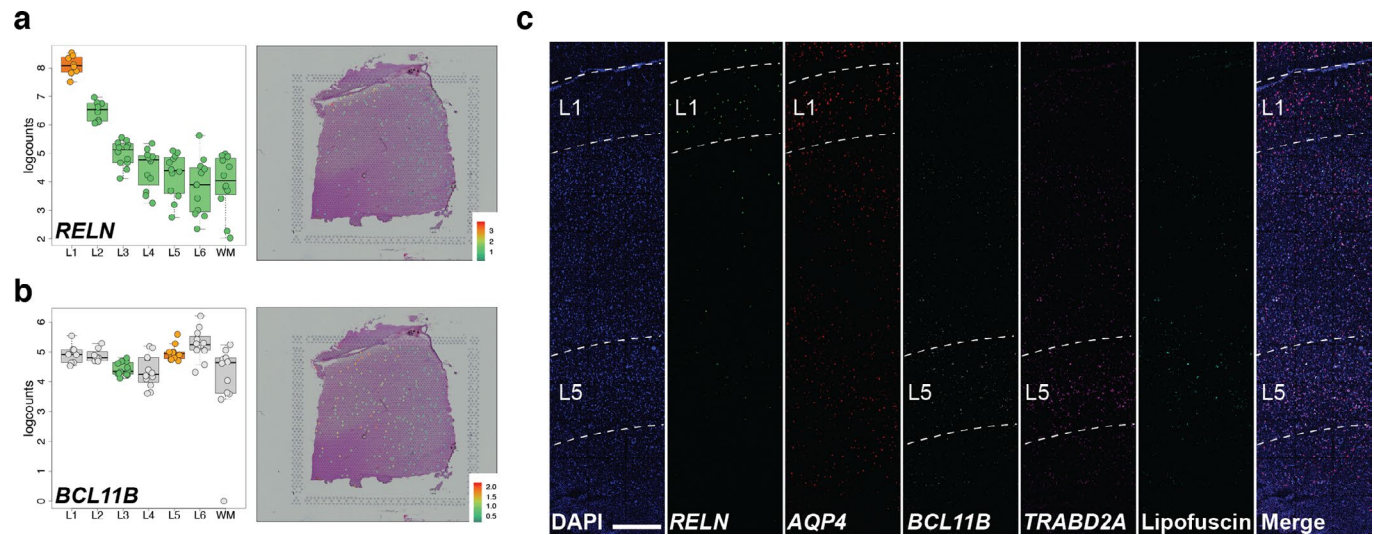
**Extended Data Fig. 5 | Known marker genes compared to the best gene, related to Results: Identifying novel layer-enriched genes in human cortex.**

Using the optimal models (Method Details: Known marker genes optimal modeling) for each known marker gene we compared the marker genes against the best gene for that given model. Results are visualized using the -log₁₀ p-values for the marker gene (y-axis) against the best gene for that model (x-axis). Points are colored by the -log₁₀ rank percentile of that gene in such a way that the top ranked gene is -log₁₀(1/22,331) and colored in yellow.

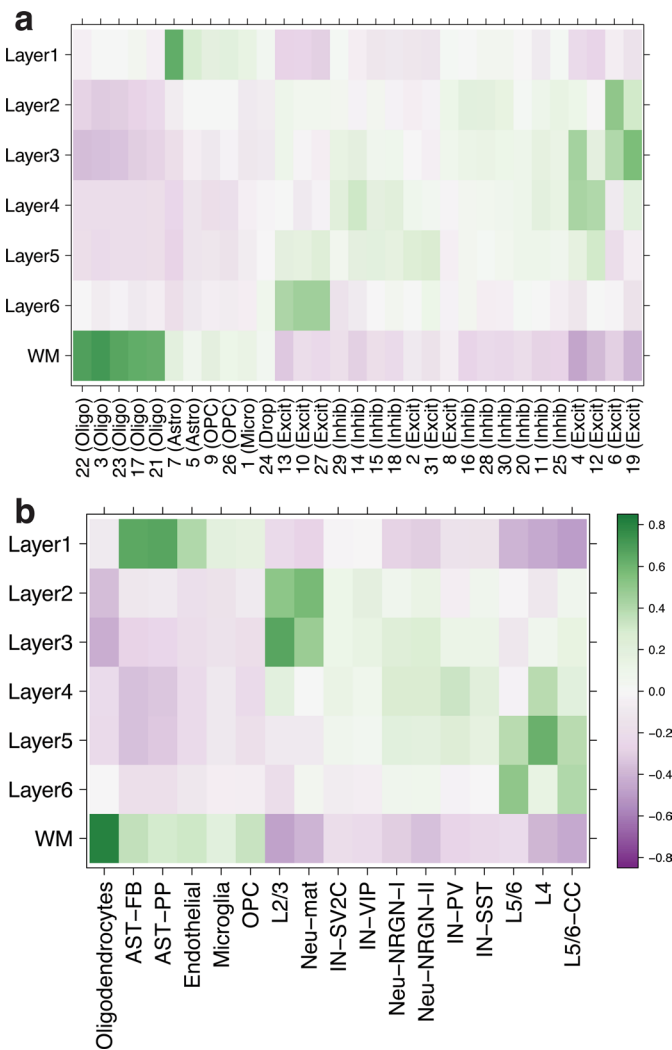


Extended Data Fig. 6 | See next page for caption.

Extended Data Fig. 6 | Replication of Visium layer-enriched genes by Allen Brain Atlas *in situ* hybridization (ISH) data, Related to Fig. 3. a-f. Left panels: Boxplots of log-transformed normalized expression (logcounts) for genes *CUX2* (**a**, L2 > L6, $p = 3.75e-19$), *ADCYAP1* (**b**, L3>rest, $p = 3.57e-08$), *RORB* (**c**, L4 > rest, $p = 2.91e-07$), *PCP4* (**d**, L5 > rest, $p = 1.81e-19$), *NTNG2* (**E**, L6>rest, $p = 5.22e-13$), and *MBP* (**f**, WM>rest, $p = 1.71e-20$). Middle panels: Spotplots of log-transformed normalized expression (logcounts) for sample 151673 for *CUX2* (**a**), *ADCYAP1* (**b**), *RORB* (**c**), *PCP4* (**d**), *NTNG2* (**e**), and *MBP* (**f**). Right panels: *in situ* hybridization (ISH) images from DLPFC (**a**, **c**, **d**, **e**, **f**) or frontal cortex (**b**) of adult human brain from Allen Brain Institute's Human Brain Atlas: <http://human.brain-map.org/>³³. Scale bar for Allen Brain Atlas ISH images = 1.6 mm. 76 pseudo-bulked layers were used for computing the statistics in **a-f**.

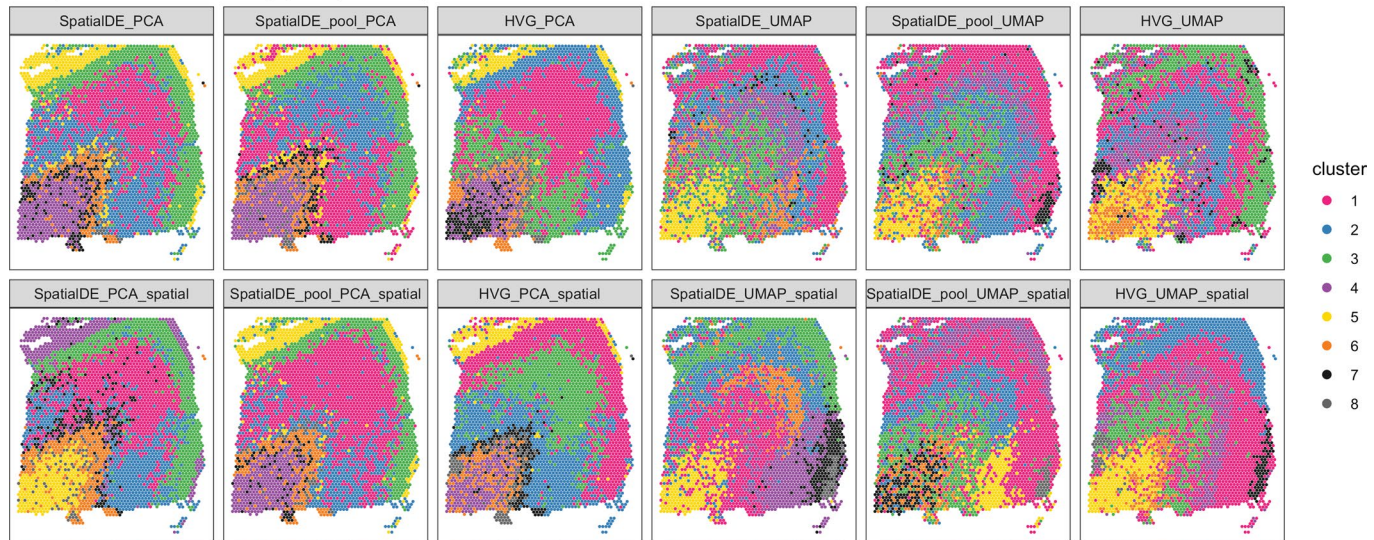


Extended Data Fig. 7 | smFISH validation of L1- and L5-enriched genes, related to Fig. 4. **a,b**, Left panels: Boxplots of log-transformed normalized expression (logcounts) for previously identified L1 and L5 marker genes *RELN* (**a**, L1>rest, $p = 7.94\text{e-}15$) and *BCL11B* (**b**, L5>L3, $p = 4.44\text{e-}02$), respectively. Right panels: Spotplots of log-transformed normalized expression (logcounts) for sample 151673 for genes *RELN* (**a**) and *BCL11B* (**b**). Corresponding boxplots and spotplots for Visium-identified genes *AQP4* and *TRABD2A* in Fig. 4. **c**, Multiplex single molecule fluorescent in situ hybridization (smFISH) in a cortical strip of DLPFC. Maximum intensity confocal projections depicting expression of DAPI (nuclei), *RELN* (L1), *AQP4* (L1), *BCL11B* (L5), *TRABD2A* (L5) and lipofuscin autofluorescence. Merged image without lipofuscin autofluorescence. Scale bar = 500 μm. 76 pseudo-bulked layers were used for computing the statistics in **a, b**.



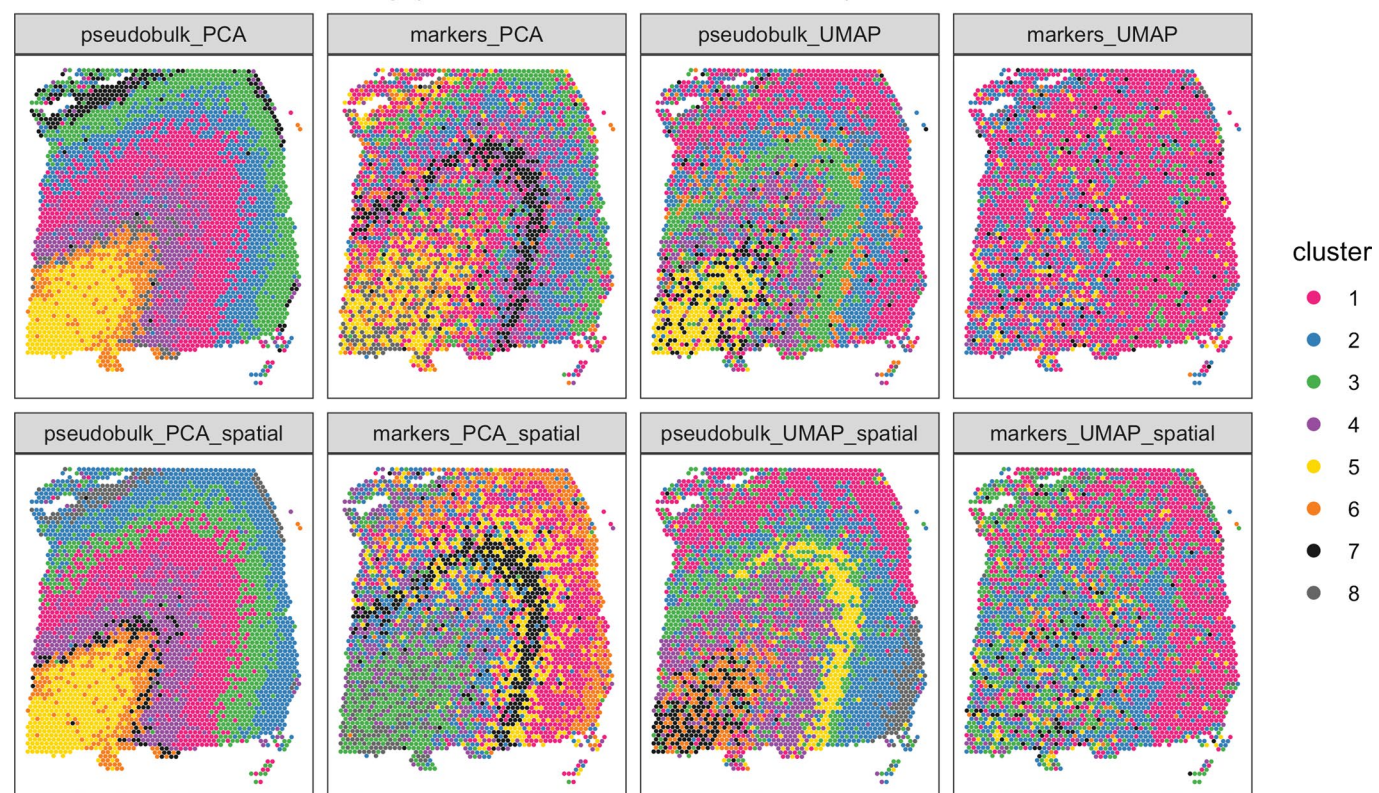
Extended Data Fig. 8 | Spatial registration of snRNA-seq data, related to Fig. 5. Heatmaps of Pearson correlation values evaluating the relationship between our Visium-derived layer-enriched statistics (y-axis) for 700 genes and **a**, Data from DLPFC from two donors, with data-driven cluster numbers and broad cell classes on the x-axis. **b**, Data from Velmeshev *et al.* with data-driven clusters provided in their processed data.

Sample 151673: Clustering (unsupervised)



Extended Data Fig. 9 | ‘Unsupervised’ clustering results for sample 151673, related to Fig. 7. Visualization of clustering results for ‘unsupervised’ methods (Supplementary Table 10) for sample 151673. Each panel displays clustering results from one clustering method. Rows display methods either without (top row) or with (bottom row) spatial coordinates included as additional features for clustering. A complete description of the different combinations of methodologies implemented in the clustering methods is provided in Supplementary Table 10.

Sample 151673: Clustering (semi-supervised and markers)



Extended Data Fig. 10 | 'Semi-supervised' and 'markers' clustering results for sample 151673, related to Fig. 7. Visualization of clustering results for 'semi-supervised' and known 'markers' gene set-based methods (Supplementary Table 10) for sample 151673. Each panel displays clustering results from one clustering method. Rows display methods either without (top row) or with (bottom row) spatial coordinates included as additional features for clustering. A complete description of the different combinations of methodologies implemented in the clustering methods is provided in Supplementary Table 10.

Reporting Summary

Nature Research wishes to improve the reproducibility of the work that we publish. This form provides structure for consistency and transparency in reporting. For further information on Nature Research policies, see our [Editorial Policies](#) and the [Editorial Policy Checklist](#).

Statistics

For all statistical analyses, confirm that the following items are present in the figure legend, table legend, main text, or Methods section.

n/a Confirmed

- The exact sample size (n) for each experimental group/condition, given as a discrete number and unit of measurement
- A statement on whether measurements were taken from distinct samples or whether the same sample was measured repeatedly
- The statistical test(s) used AND whether they are one- or two-sided
Only common tests should be described solely by name; describe more complex techniques in the Methods section.
- A description of all covariates tested
- A description of any assumptions or corrections, such as tests of normality and adjustment for multiple comparisons
- A full description of the statistical parameters including central tendency (e.g. means) or other basic estimates (e.g. regression coefficient) AND variation (e.g. standard deviation) or associated estimates of uncertainty (e.g. confidence intervals)
- For null hypothesis testing, the test statistic (e.g. F , t , r) with confidence intervals, effect sizes, degrees of freedom and P value noted
Give P values as exact values whenever suitable.
- For Bayesian analysis, information on the choice of priors and Markov chain Monte Carlo settings
- For hierarchical and complex designs, identification of the appropriate level for tests and full reporting of outcomes
- Estimates of effect sizes (e.g. Cohen's d , Pearson's r), indicating how they were calculated

Our web collection on [statistics for biologists](#) contains articles on many of the points above.

Software and code

Policy information about [availability of computer code](#)

Data collection	The Space Ranger tool from 10x Genomics was used to process the raw sequencing reads and histology imaging data
Data analysis	<p>The code used for this project is available at https://github.com/LieberInstitute/HumanPilot and archived through Zenodo at https://doi.org/10.5281/zenodo.3691916. The software developed as part of this project, spatialLIBD, is available through Bioconductor at bioconductor.org/packages/spatialLIBD and GitHub at https://github.com/LieberInstitute/spatialLIBD.</p> <p>Here's a list of software used:</p> <ul style="list-style-type: none"> * SpaceRanger version 1.0.0 from 10X Genomics (uses STAR v2.5.1b) with refdata-cellranger-GRCh38-3.0.0 annotation files. * rgbd2lab and imsegkmeans from MATLAB version R2019a. * SingleCellExperiment (1.8.0), scran (1.14.5), scater (1.14.3), spatialLIBD (0.99.0), shiny (1.4.0), plotly (4.9.2), igraph (1.2.4.1), limma (3.42.0), BiocSingular (1.2.2), and uwot (0.1.5) R software packages matching Bioconductor version 3.10 from R 3.6. Version numbers extracted from scripts such as https://github.com/LieberInstitute/HumanPilot/blob/master/Analysis/Layer_Guesses/layer_specificity.R#L1724. * Zen version "Black" https://www.zeiss.com/content/dam/Microscopy/Downloads/Pdf/FAQs/zen-version-investigator.pdf. * dotdotdot from git commit with hash ID 4e1350b from https://github.com/LieberInstitute/dotdotdot/tree/4e1350b027f5457f2e96e562cfa80c6752461478. * Cell Ranger version 3.0.2 from 10X Genomics. * LDSC version 1.0.1. * MAGMA version 1.07b. * SpatialDE version 1.1.0 with Python v3.8.0.

For manuscripts utilizing custom algorithms or software that are central to the research but not yet described in published literature, software must be made available to editors and reviewers. We strongly encourage code deposition in a community repository (e.g. GitHub). See the Nature Research [guidelines for submitting code & software](#) for further information.

Data

Policy information about [availability of data](#)

All manuscripts must include a [data availability statement](#). This statement should provide the following information, where applicable:

- Accession codes, unique identifiers, or web links for publicly available datasets
- A list of figures that have associated raw data
- A description of any restrictions on data availability

Processed data is publicly available from the Bioconductor package spatialLIBD <http://bioconductor.org/packages/spatialLIBD> and <https://github.com/LieberInstitute/spatialLIBD>.

The raw data is publicly available from the Globus endpoint “jhpc#HumanPilot10x” that is also listed at <http://research.libd.org/globus/>. The raw data provided through Globus includes all the FASTQ files and raw image files. External data used in this project is detailed under “Methods: snRNA-seq spatial registration” as well as “Methods: Clinical gene set enrichment analyses”.

Field-specific reporting

Please select the one below that is the best fit for your research. If you are not sure, read the appropriate sections before making your selection.

Life sciences Behavioural & social sciences Ecological, evolutionary & environmental sciences

For a reference copy of the document with all sections, see nature.com/documents/nr-reporting-summary-flat.pdf

Life sciences study design

All studies must disclose on these points even when the disclosure is negative.

Sample size	No statistical methods were used to pre-determine sample sizes, but our sample sizes are greater than previous publications with the earlier Spatial Transcriptomics technology that preceded Visium (DOLs: 10.1126/science.aaf2403 and 10.1126/science.aav9776).
	Three high quality donors similar in age and primary diagnosis (all three are neurotypical controls) were selected for this study. Two are males and one is a female, with age at time of death from 30 to 46 years of age.
Data exclusions	No data was excluded from the analyses. All aligned RNA-seq reads were used and all Visium spots were used, as typical scRNA-seq quality control metrics were related to the DLPFC layers.
Replication	Spatially-adjacent replicates were obtained for all donor brains. Furthermore, for each donor, we obtained two pairs of spatially-adjacent replicates at a 300 micron distance between the pairs as shown in Figure 1. We verified that the spatial replicates samples clustered with each other as described in the Methods.
Randomization	Samples were not randomized. We used the “block” argument in the analysis methods from scran for the 6 pairs of spatially-adjacent replicates as explained in the Methods: spot-level data processing. Given the sample size (3 donors) we did not adjust statistically for covariates such as sex and age.
Blinding	Data collection and analysis were not performed blind to the conditions of the experiments.

Reporting for specific materials, systems and methods

We require information from authors about some types of materials, experimental systems and methods used in many studies. Here, indicate whether each material, system or method listed is relevant to your study. If you are not sure if a list item applies to your research, read the appropriate section before selecting a response.

Materials & experimental systems

n/a	Involved in the study
<input checked="" type="checkbox"/>	<input type="checkbox"/> Antibodies
<input checked="" type="checkbox"/>	<input type="checkbox"/> Eukaryotic cell lines
<input checked="" type="checkbox"/>	<input type="checkbox"/> Palaeontology and archaeology
<input checked="" type="checkbox"/>	<input type="checkbox"/> Animals and other organisms
<input type="checkbox"/>	<input checked="" type="checkbox"/> Human research participants
<input checked="" type="checkbox"/>	<input type="checkbox"/> Clinical data
<input checked="" type="checkbox"/>	<input type="checkbox"/> Dual use research of concern

Methods

n/a	Involved in the study
<input checked="" type="checkbox"/>	<input type="checkbox"/> ChIP-seq
<input checked="" type="checkbox"/>	<input type="checkbox"/> Flow cytometry
<input checked="" type="checkbox"/>	<input type="checkbox"/> MRI-based neuroimaging

Human research participants

Policy information about [studies involving human research participants](#)

Population characteristics

Describe the covariate-relevant population characteristics of the human research participants (e.g. age, gender, genotypic information, past and current diagnosis and treatment categories). If you filled out the behavioural & social sciences study design questions and have nothing to add here, write "See above."

Recruitment

Describe how participants were recruited. Outline any potential self-selection bias or other biases that may be present and how these are likely to impact results.

Ethics oversight

Identify the organization(s) that approved the study protocol.

Note that full information on the approval of the study protocol must also be provided in the manuscript.